

Accepted Manuscript

Oxygen isotopic compositions of allende type C CAIs: evidence for isotopic exchange during nebular melting and asteroidal metamorphism

A.N. Krot, M. Chaussidon, H. Yurimoto, N. Sakamoto, K. Nagashima, I.D. Hutcheon, G.J. MacPherson

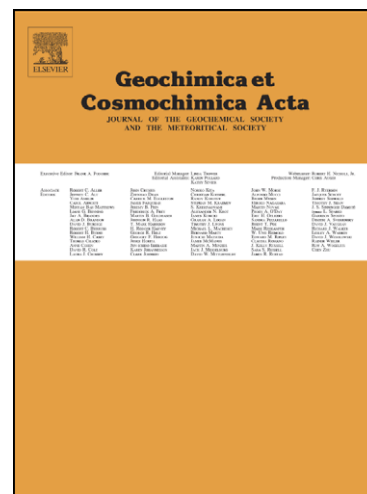
PII: S0016-7037(08)00084-7
DOI: [10.1016/j.gca.2008.02.011](https://doi.org/10.1016/j.gca.2008.02.011)
Reference: GCA 5554

To appear in: *Geochimica et Cosmochimica Acta*

Received Date: 5 March 2007
Accepted Date: 11 February 2008

Please cite this article as: Krot, A.N., Chaussidon, M., Yurimoto, H., Sakamoto, N., Nagashima, K., Hutcheon, I.D., MacPherson, G.J., Oxygen isotopic compositions of allende type C CAIs: evidence for isotopic exchange during nebular melting and asteroidal metamorphism, *Geochimica et Cosmochimica Acta* (2008), doi: [10.1016/j.gca.2008.02.011](https://doi.org/10.1016/j.gca.2008.02.011)

This is a PDF file of an unedited manuscript that has been accepted for publication. As a service to our customers we are providing this early version of the manuscript. The manuscript will undergo copyediting, typesetting, and review of the resulting proof before it is published in its final form. Please note that during the production process errors may be discovered which could affect the content, and all legal disclaimers that apply to the journal pertain.



**OXYGEN ISOTOPIC COMPOSITIONS OF ALLENDE TYPE C CAIs:
EVIDENCE FOR ISOTOPIC EXCHANGE DURING NEBULAR MELTING AND
ASTEROIDAL METAMORPHISM**

A. N. Krot^{1*}, M. Chaussidon², H. Yurimoto³, N. Sakamoto³, K. Nagashima¹,
I. D. Hutcheon⁴ and G. J. MacPherson⁵

¹Hawai'i Institute of Geophysics and Planetology, School of Ocean and Earth Science and Technology, University of Hawai'i at Manoa, Honolulu, HI 96822, USA. *e-mail address: sasha@higp.hawaii.edu

²Centre de Recherches Pétrographiques et Géochimiques, CNRS-UPR 2300, BP20, 54501 Vandoeuvre les Nancy, France

³Division of Earth and Planetary Sciences, Hokkaido University, Sapporo 060-0810, Japan

⁴Glenn T. Seaborg Institute, Lawrence Livermore National Laboratory, Livermore, CA 94451, USA

⁵Smithsonian Institution, Department of Mineral Sciences, NHB 119, Washington DC 20560, USA

submitted to *Geochimica et Cosmochimica Acta* March 5, 2007

revised: February 10, 2007

accepted for publication February 12, 2008

ABSTRACT. *In situ* oxygen isotopic measurements of primary and secondary minerals in Type C CAIs from the Allende CV3 chondrite reveal that the pattern of relative enrichments and depletions of ^{16}O in the primary minerals within each individual CAI are similar to the patterns observed in Types A and B CAIs from the same meteorite. Spinel is consistently the most ^{16}O -rich ($\Delta^{17}\text{O} = -25\text{‰}$ to -15‰), followed by Al,Ti-dioside ($\Delta^{17}\text{O} = -20\text{‰}$ to -5‰) and anorthite ($\Delta^{17}\text{O} = -15\text{‰}$ to 0‰). Melilite is the most ^{16}O -depleted primary mineral ($\Delta^{17}\text{O} = -5\text{‰}$ to -3‰). We conclude that the original melting event that formed Type C CAIs occurred in a ^{16}O -rich ($\Delta^{17}\text{O} \leq -20\text{‰}$) nebular gas and they subsequently experienced oxygen isotopic exchange in a ^{16}O -poor reservoir. At least three of these (*ABC*, *TS26F1* and *93*) experienced remelting at the time and place where chondrules were forming, trapping and partially assimilating ^{16}O -poor chondrule fragments. The observation that the pyroxene is ^{16}O -rich relative to the feldspar, even though the feldspar preceded it in the igneous crystallization sequence, disproves the class of CAI isotopic exchange models in which partial melting of a ^{16}O -rich solid in a ^{16}O -poor gas is followed by slow crystallization in that gas. For the typical (not associated with chondrule materials) Type C CAIs as well for as the Types A and B CAIs, the exchange that produced internal isotopic heterogeneity within each CAI must have occurred largely in the solid state. The secondary phases grossular, monticellite, and forsterite commonly have similar oxygen isotopic compositions to the melilite and anorthite they replace, but in one case (CAI *160*) grossular is ^{16}O -enriched ($\Delta^{17}\text{O} = -10\text{‰}$ to -6‰) relative to melilite ($\Delta^{17}\text{O} = -5\text{‰}$ to -3‰), meaning that the melilite and anorthite must have exchanged its oxygen subsequent to secondary alteration. This isotopic exchange in melilite and anorthite likely occurred on the CV parent asteroid, possibly during fluid-assisted thermal metamorphism.

INTRODUCTION

Oxygen isotope compositions of primitive Solar System materials preserve a detailed record of diverse nebular and asteroidal processes. The earliest high temperature events are best revealed in calcium-aluminum-rich inclusions (CAIs) in chondritic meteorites. CAIs in the least equilibrated primitive chondrites (e.g., CR2, CO3.0 and the ungrouped carbonaceous chondrite Acfer 094) generally have uniformly ^{16}O -rich ($\Delta^{17}\text{O} \leq -20\text{‰}$) compositions (Aléon et al., 2002; Itoh et al., 2004; Fagan et al., 2007a) coupled with large excesses of ^{26}Mg ($^{26}\text{Mg}^*$) from the decay of extinct ^{26}Al ($t_{1/2} = 0.73$ Myr), which together indicate early CAI formation in an ^{16}O -rich gaseous reservoir (e.g., MacPherson et al., 1995; Krot et al., 2002). In contrast, the CAIs from more “processed” chondrites (e.g., CV3) preserve a more complex and prolonged history. Although CV3 CAIs also formed very early (Amelin et al., 2002; Thrane et al., 2006), most of them experienced later partial isotopic exchange in the presence of an ^{16}O -poor reservoir (Clayton et al., 1977). This exchange resulted in large oxygen isotopic heterogeneity within individual CAIs: melilite and anorthite typically are ^{16}O -depleted ($\Delta^{17}\text{O} > -10\text{‰}$) relative to spinel and Al,Ti-diopside, which largely retain their original ^{16}O -rich compositions (e.g., Clayton et al., 1977; McKeegan et al., 1998; Aléon et al., 2005a,b). Only rare patches within some melilite and anorthite grains in Allende CAIs do retain ^{16}O -rich compositions (e.g., Yurimoto et al., 1998; Yoshitake et al., 2002; Harazono and Yurimoto, 2003; Kim et al., 2002; Ito et al., 2004; Fagan et al., 2004; Aléon et al., 2005b), testifying to their original ^{16}O -rich composition.

Several mechanisms have been proposed to explain the nature of the selective isotopic exchange in melilite and anorthite, but all have some problems. (i) High-temperature gas-solid exchange in the solar nebula (Clayton et al., 1977) is inconsistent with the measured oxygen self-diffusion rates in melilite, anorthite, diopside and spinel (Yurimoto et al., 1989; Ryerson and McKeegan, 1994). (ii) Isotopic exchange between the ^{16}O -rich CAI melt and an ^{16}O -poor nebular gas either during CAI melting or crystallization is difficult to reconcile with the inferred crystallization sequence of CAI melts (Stolper, 1982; Stolper and Paque, 1986). (iii) Isotopic exchange during disequilibrium melting (Yurimoto et al., 1998; Greenwood, 2004) has yet to be reproduced experimentally. (iv) Isotopic exchange during relatively low-temperature alteration in the presence of fluid phase on the CV parent asteroid or in the solar nebula has been advocated by several researchers (e.g., Krot et al., 1998; Jabeen et al., 1998a,b, 1999; Ash et al., 1999; Young et al., 1999; Ash and Young, 2000; Nagashima et al., 2007). The lack of experimental

data on the diffusion rates of oxygen in CAI-like minerals in the presence of aqueous solution does not allow us to test this hypothesis yet.

Olivine-rich objects that have not been melted, such as amoeboid olivine aggregates (AOAs), likewise originated in a ^{16}O -rich environment (Hiyagon and Hashimoto, 1999; Krot et al., 2002). Chondrules, however, almost uniformly are ^{16}O -depleted relative to AOAs and CAIs. The most ^{16}O -rich varieties are Al-rich chondrules, which can have $\Delta^{17}\text{O} \simeq -5\text{‰}$ to -10‰ (e.g., Russell et al., 2000). Chondrules also show consistently lower $^{26}\text{Mg}^*$ than do CAIs (e.g., Kita et al., 2005 and references therein). Their collective oxygen and magnesium isotopic signatures indicate that chondrules were melted 1-3 million years after CAI formation and that melting occurred in a ^{16}O -depleted environment (Krot et al., 2005a).

The petrogenetic reason(s) underlying the isotopic differences between chondrules and CAIs is not well understood, and resolving this problem is very important for understanding early Solar System evolution. One way to approach the problem is to study objects that have transitional properties between chondrules and CAIs. Al-rich chondrules are one such kind of intermediate object, and these have received much attention over the past 10 years (e.g., Russell et al., 1996, 2000; Huss et al., 2001; MacPherson and Huss, 2005; Tronche et al., 2007). Another group of “intermediate” objects are the Type C CAIs, which are rare relative to other CAI varieties and which have been little studied (Wark, 1987). Their bulk compositions are close to those of many Al-rich chondrules (MacPherson and Huss, 2005) and, like the latter, deviate significantly from the predictions of equilibrium condensation of a hot solar gas (Beckett and Grossman, 1988; Yoneda and Grossman, 1995; see discussion by MacPherson and Huss, 2005).

This study is part of our on-going program to document the properties of this important group of objects, from different chondrite groups. We previously showed that Type C CAIs from Allende experienced complex formation histories, involving multiple episodes of nebular melting and post-crystallization alteration (Krot et al., 2005b, 2007a,b). Particularly noteworthy was the finding that some of the Type C CAIs were remelted in a location where ferromagnesian dust was abundant, possibly during the chondrule melting process (Krot et al., 2005b, 2007a). In order to better understand the setting and conditions of nebular melting of the Type C CAIs, as well as later (asteroidal?) alteration, we report here the oxygen isotopic compositions of seven Allende Type C CAIs, named #160, #100, #6-1-72, CG5, #93, ABC and TS26F1. Prior to this study, only one other Type C CAI (also from Allende) had been analyzed for oxygen isotopes (Imai and Yurimoto, 2000).

ANALYTICAL TECHNIQUES

Polished thin and thick sections of all CAIs were studied using optical microscopy, X-ray elemental mapping, backscattered electron (BSE) imaging, electron probe microanalysis (EPMA), and secondary ion mass-spectrometry (SIMS). The BSE images were obtained with a JEOL JSM-5900LV scanning electron microscope. This instrument is equipped with a Thermo Electron energy dispersive spectrometer (EDS), which was operated at 15-20 kV accelerating voltage and 1-2 nA beam current. Element X-ray area maps having a spatial resolution of 1-10 $\mu\text{m}/\text{pixel}$ were acquired using five spectrometers of a Cameca SX-50 microprobe, operated at 15 keV accelerating voltage, 50-100 nA beam current, and $\sim 1\text{-}2\ \mu\text{m}$ beam size. The element maps for Mg, Ca and Al (all $K\alpha$) were combined using a RGB-color scheme and the commercial software package ENVI (ENvironment for Visualizing Images). Quantitative mineral analyses were also acquired using the Cameca SX-50, via wavelength dispersive X-ray spectroscopy with operating conditions of 15 keV accelerating voltage, 10-20 nA beam current, and $\sim 1\text{-}2\ \mu\text{m}$ beam size. For each element, counting times on both peak and background were 30 sec (10 sec for Na and K). Bulk compositions of chondrules were measured using a defocused $\sim 10\ \mu\text{m}$ beam. Matrix effects were corrected using the PAP procedure (Pouchou and Pichoir, 1984). The detection limits are: 0.03 wt% for SiO_2 , Al_2O_3 , MgO , and CaO ; 0.04 wt% for TiO_2 , Cr_2O_3 , and K_2O ; 0.06 wt% for Na_2O ; and 0.07 wt% for MnO and FeO .

Oxygen isotopic compositions were measured *in situ* using the Cameca ims-1270 ion microprobes at CRPG-CNRS (Nancy) and Hokkaido University (HU), and the Cameca ims-1280 ion microprobe at the University of Hawai'i (UH).

In Nancy, oxygen isotopic data were collected in multicollection mode. ^{16}O and ^{18}O were measured using Faraday cups (FC); ^{17}O was measured using the axial electron multiplier (EM). A Cs^+ primary beam of 10 nA was used to produce ion probe sputter pits approximately 25-30 μm in diameter. At these conditions, the count rate was $\sim 2 \times 10^6\ \text{sec}^{-1}$ for ^{18}O . A normal-incidence electron gun was used for charge compensation of analyzed areas. Corrections for instrumental mass fractionation (IMF), counting statistics, and uncertainty in standard compositions were applied. The IMF was corrected using terrestrial olivine (San Carlos) and diopside standards (for details, see Gurenko and Chaussidon, 2002). The precision (2σ) of individual oxygen isotopic analyses obtained with this instrument is better than 1.5‰ for both $\delta^{18}\text{O}$ and $\delta^{17}\text{O}$.

At HU, a primary ion beam of mass filtered Cs^+ ions accelerated to 20 keV was used to

excavate shallow pits ranging from 3 to 10 μm in diameter. The primary current was adjusted for each measurement to obtain a count rate for $^{16}\text{O}^-$ ions of ~ 3.5 to $4 \times 10^5 \text{ sec}^{-1}$. Again, a normal-incidence electron gun was used for charge compensation of analyzed areas. Negative secondary ions from the $^{16}\text{O}^-$ tail, $^{16}\text{O}^-$, $^{17}\text{O}^-$, $^{16}\text{OH}^-$, and $^{18}\text{O}^-$ were analyzed at a mass resolving power ($m/\Delta m$) of ~ 6000 , sufficient to completely separate $^{16}\text{OH}^-$ interference on $^{17}\text{O}^-$. Secondary ions were detected by a monocollector EM in pulse counting mode, and analyses were corrected for dead time. The IMF was corrected using terrestrial mineral standards: SPU spinel (from Russia), anorthite (Miyake-jima, Japan), augite (Takashima, Japan), and synthetic gehlenite and åkermanite. The reproducibility of $^{17}\text{O}/^{16}\text{O}$ and $^{18}\text{O}/^{16}\text{O}$ on different analysis points from the same standard was $\sim \pm 5\%$ (2σ). Matrix effects on detected oxygen isotopic compositions among the minerals analyzed are also limited to about $\pm 5\%$. Therefore, we used one standard, the SPU spinel, to determine IMF during each analytical session. Overall errors are estimated to be about $\pm 7.5\%$ for each analysis.

At UH, a 2-3 nA focused Cs^+ primary ion beam was rastered over a 25×25 micron area for 120-150 seconds. The raster was then reduced to 10×10 microns and data collected for 4 sec \times 40 cycles. The ion microprobe was operated at -10 keV with a 50 eV energy window. $^{16}\text{O}^-$ was measured on multicollector FC L'2 with 10^{10} ohm resistor; $^{18}\text{O}^-$ was measured on FC H1 with 10^{11} ohm resistor, and $^{17}\text{O}^-$ was measured with the monocollector EM. The MRP for $^{16}\text{O}^-$ and $^{18}\text{O}^-$ was ~ 2000 , and that for $^{17}\text{O}^-$ was ~ 5500 , sufficient to separate interfering $^{16}\text{OH}^-$. The normal-incidence electron flood gun was used for charge compensation. All data were corrected for IMF using synthetic forsterite and olivine from the Brenham pallasite. Under the analytical conditions employed, the total precision (2σ) of individual oxygen isotopic analyses is $\sim 1.5\%$ for both $\delta^{18}\text{O}$ and $\delta^{17}\text{O}$. Because IMF for spinel, Al,Ti-diopside, anorthite and melilite may be different for the UH Cameca ims-1280 (e.g., Kita et al., 2007), it may result in larger uncertainty in $\delta^{18}\text{O}$.

Oxygen isotopic compositions are reported herein as per mil deviations from SMOW (Standard Mean Ocean Water), using the conventional notation:

$$\delta^{18}\text{O} = [({}^{18}\text{O}/{}^{16}\text{O}_{\text{unknown}}) / ({}^{18}\text{O}/{}^{16}\text{O}_{\text{SMOW}}) - 1] * 1000$$

$$\delta^{17}\text{O} = [({}^{17}\text{O}/{}^{16}\text{O}_{\text{unknown}}) / ({}^{17}\text{O}/{}^{16}\text{O}_{\text{SMOW}}) - 1] * 1000$$

$$\Delta^{17}\text{O} = \delta^{17}\text{O} - 0.52 \times \delta^{18}\text{O}.$$

Following oxygen isotopic measurements, each CAI analyzed was re-examined in BSE and

secondary electron images to verify the locations of the sputtered craters and mineralogy of the phases analyzed.

SAMPLE DESCRIPTION

Detailed mineralogical and petrographic descriptions of all the CAIs studied herein are given in Wark (1987) and Krot et al. (2007a,b). Here, we briefly summarize the major mineralogical characteristics of these CAIs important for understanding their oxygen isotopic compositions. Additional X-ray elemental maps illustrating the overall mineralogy of the CAIs are included in an electronic annex (EA).

Based on mineralogy and petrography, Krot et al. (2007a,b) divided Allende Type C CAIs into three groups:

(1) CAIs with melilite, Al,Ti-diopside in both massive and highly poikilitic (enclosing anorthite; the “lacy” texture of Wark (1987) forms, both in a fine-grained anorthite groundmass (#6-1-72, #100, #160),

(2) CAI *CG5* with massive melilite, Al,Ti-diopside and anorthite, and exceedingly abundant fine-grained spinel,

(3) CAIs associated with chondrule material – either containing chondrule fragments in their peripheries (*ABC*, *TS26F1*) or surrounded by chondrule-like, igneous rims (#93).

CAI #160 is a fragment, partly surrounded by a Wark-Lovering rim sequence of spinel, Al,Ti-diopside and olivine (Figs. 1, 1EA). The interior consists of Al,Ti-diopside, melilite, and spinel in an anorthite matrix. The pyroxene occurs as spongy crystals that poikilitically enclose myriad tiny anorthite grains, less commonly as massive grains poikilitically enclosing euhedral spinel, and as interstitial grains between polycrystalline melilite. Melilite occurs as spongy grains poikilitically enclosing tiny anorthite grains and as compact, polycrystalline regions. The spongy melilite grains are pseudomorphed to varying degrees by grossular, monticellite and forsterite. Melilite and anorthite in the outer portion of the CAI are extensively replaced by nepheline and sodalite.

CAI #100 (Figs. 2, 2EA) consists of four fragments (hereafter “*100a*”, “*100b*”, “*100c*” and “*100d*”), each composed of melilite, Al,Ti-diopside, spinel, and fine-grained anorthite groundmass. The petrographic context of the fragments is unknown; none of them have Wark-Lovering rim layers or matrix material attached. There are, however, significant variations in the morphology of Al,Ti-diopside and melilite grains among the fragments, possibly reflecting their different position within the CAI. Al,Ti-diopside occurs as coarse (100-200 μm in size) euhedral but highly spongy (poikilitic) grains, and also as small (20-30 μm in size) nearly inclusion-free isolated crystals or aggregates. Most melilite grains have spongy, poikilitic textures. Anorthite-free, massive melilite regions are rare and are overgrown by poikilitic melilite and pyroxene; the melilite is pseudomorphically-replaced to varying degrees by grossular, monticellite and forsterite.

CAI #6-1-72 is a complete, elliptical CAI surrounded by a Wark-Lovering rim sequence of spinel, Al,Ti-diopside, and olivine (Figs. 3, 3EA). The CAI consists of two texturally distinct regions. The main portion is mineralogically similar to CAIs #100 and #160. It is composed of fine-grained groundmass anorthite and coarse-grained, poikilitic Al,Ti-diopside and melilite; spinel is relatively minor and heterogeneously distributed in the CAI. Spongy melilite is partially pseudomorphed by grossular, monticellite and forsterite. The center of this part of the CAI is free of nepheline and sodalite, in contrast to the periphery where they are common and replace anorthite and (?) melilite. The core is heavily fractured; some of the fractures are filled by andradite and wollastonite. The second portion of *6-1-72* consists of compact, polycrystalline melilite, Al,Ti-diopside, isolated spinel grains and a spinel palisade. This portion is texturally and mineralogically similar to Type B CAIs from CV chondrites (e.g., MacPherson et al., 1988). Melilite and pyroxene contain abundant inclusions of spinel, perovskite and platinum group element nuggets; neither melilite nor pyroxene have the poikilitic texture that is so prominent in the other part of the inclusion. Melilite is partially replaced along grain boundaries by grossular, monticellite, and forsterite. Coarse-grained melilite and the palisade body in outer part of the

second portion are overgrown by lacy Al,Ti-diopside.

CG5 exists now only as a fragment in a grain mount, and its original size and shape are unknown. Most of the inclusion was consumed during detailed trace element studies of Allende CAIs (e.g., Grossman and Ganapathy, 1975). This inclusion is composed of lath-shaped anorthite, Al,Ti-diopside and melilite, all poikilitically enclosing dense clouds of tiny spinel grains (Figs. 4, 4EA). Secondary minerals are absent; it is unknown if the CAI originally had a Wark-Lovering rim. Melilite and Al,Ti-diopside occur in interstitial regions between prismatic anorthite crystals and also form large, massive grains in anorthite-poor regions of the CAI.

CAI #93 (Fig. 5) is a fragment of what was originally a rounded CAI that was likely several mm or more in maximum size. The inclusion is composed of coarse-grained, Al,Ti-diopside that optically encloses, lath-shaped anorthite; euhedral Cr-bearing spinel occurs primarily in the outer portions of the CAI. Interstitial, fine-grained regions are composed of melilite, Al-diopside and anorthite. In the core, coarse-grained anorthite is largely replaced by nepheline and sodalite; in the periphery, the anorthite is replaced by sodalite, ferrous olivine and nepheline. The melilite is replaced by a fine-grained, porous material largely composed of grossular, monticellite and wollastonite; minor secondary nepheline and sodalite occur as well. The peripheral zone of the CAI is overgrown by a coarse-grained igneous region composed of augite, pigeonite and anorthitic plagioclase. Plagioclase is extensively replaced by sodalite and ferrous olivine. The coarse-grained, igneous region is separated from the CAI by a spinel-rich layer, possibly a remnant of a Wark-Lovering rim.

ABC is an angular CAI fragment enclosed within meteorite matrix. It is composed of lath-shaped anorthite and Al,Ti-diopside, both poikilitically enclosing spinel grains, and fine-grained, interstitial material (Fig. 6). Anorthite is corroded by sodalite and nepheline. The interstitial material consists of melilite, Al-diopside, grossular, wollastonite and monticellite. Relict olivine and low-Ca pyroxene grains occur in the peripheral portion of the fragment.

TS26F1 is a complete, dog-leg-shaped CAI that shows a well-defined core-mantle structure (Figs. 7, 5EA). The coarse-grained core consists of lath-shaped anorthite and euhedral, sector-zoned Al,Ti-diopside, both poikilitically enclosing spinel grains, and interstitial material. The interstitial material is composed of melilite, diopside and secondary grossular, monticellite, wollastonite, sodalite and ferrous olivine; the secondary minerals replace melilite and anorthite. The mantle is finer-grained and enriched in SiO_2 compared to the core. It is separated from the core by a discontinuous layer of Fe,Ni-sulfides and composed of Al,Ti-diopside, lath-shaped anorthite and abundant relict grains of forsteritic olivine and low-Ca pyroxene. The olivine and low-Ca pyroxene grains are extensively corroded by diopside and surrounded by haloes of augite; augite is also present in the outermost portion of the mantle.

OXYGEN ISOTOPIC COMPOSITIONS

Type C CAIs with spongy (poikilitic) melilite and Al,Ti-diopside

In CAI *160* (Fig. 1), oxygen isotopes were measured in both spongy and massive textural types of melilite and Al,Ti-diopside, as well as spinel, anorthite groundmass and a fine-grained mixture of grossular+monticellite replacing spongy melilite (Table 1, Figs. 8a,b). In Figure 8a, the data are plotted as $\delta^{17}\text{O}$ vs. $\delta^{18}\text{O}$. To illustrate variations in oxygen isotopic compositions of individual minerals, the same data, grouped by minerals, are plotted in Figure 8b as $\Delta^{17}\text{O} = \delta^{17}\text{O} - 0.52 \times \delta^{18}\text{O}$. Spinel and massive Al,Ti-diopside grains are similarly ^{16}O -enriched ($\Delta^{17}\text{O} = -24\text{‰}$ to -23‰) relative to spongy Al,Ti-diopside ($\Delta^{17}\text{O} = -20\text{‰}$ to -17‰). The apparent ^{16}O -depletion of spongy Al,Ti-diopside is almost certainly due to small inclusions of ^{16}O -depleted anorthite,

which shows a wide compositional range ($\Delta^{17}\text{O} = -10\text{‰}$ to -2‰). Massive melilite and spongy melilite have similar, ^{16}O -poor compositions ($\Delta^{17}\text{O} = -5\text{‰}$ to -3‰). The grossular-monticellite intergrowths are ^{16}O -enriched ($\Delta^{17}\text{O} = -10\text{‰}$ to -6‰) relative to the spongy melilite they replace, suggesting that the alteration of the melilite occurred prior to the melilite acquiring its ^{16}O -poor composition.

In CAI 100 (Fig. 2), oxygen isotopes were measured in both spongy and massive melilite, three textural occurrences of Al,Ti-diopside (spongy, small euhedral grains, and a compact aggregate of grains), spinel, anorthite groundmass, and fine-grained secondary forsterite + monticellite + grossular using both the CNRS/CRPG and HU ion microprobes (Table 1, Fig. 9). There is reasonable agreement between the two data sets, but they have different error bars and are plotted separately. Spongy Al,Ti-diopside grains are slightly ^{16}O -depleted ($\Delta^{17}\text{O} = -18\text{‰}$ to -17‰) relative to spinel ($\Delta^{17}\text{O} = -25\text{‰}$) and also relative to the compositionally-similar small, euhedral Al,Ti-diopside grains ($\Delta^{17}\text{O} = -21\text{‰}$ to -16‰) and grain aggregates ($\Delta^{17}\text{O} = -18\text{‰}$). Again, the observed range in oxygen isotopic composition of Al,Ti-diopside and the relative ^{16}O -depletion of the spongy grains are probably due to the numerous enclosed small anorthite grains that were sputtered during ion probe analyses (see, e.g., spots 87, 88, 92 and 93 in Figs. 2a-c). Although ion probe analyses of pure Al,Ti-diopside collected by the HU ims-1270 show a relatively large spread in $\Delta^{17}\text{O}$ (-23‰ to -15‰), these analyses have larger error bars ($\pm 5\text{‰}$, 2σ) than and are within 2σ error of the CNRS/CRPG data (Fig. 9). Fine-grained anorthite shows a wide compositional range ($\Delta^{17}\text{O} = -14\text{‰}$ to -4‰), even discounting those spots contaminated by tiny inclusions of spinel and Al,Ti-diopside (Table 1). Melilite grains of massive (Fig. 2d) and spongy (Fig. 2e) textures have similar, ^{16}O -poor compositions ($\Delta^{17}\text{O} = -5\text{‰}$ to -3‰). Secondary grossular, monticellite and forsterite, which collectively replace spongy melilite (Figs. 2d-f), have ^{16}O -poor compositions ($\Delta^{17}\text{O} = -9\text{‰}$, -2‰ , and -3‰ to -5‰ , respectively; $\pm 5\text{‰}$ 2σ errors), comparable with melilite.

In CAI 6-1-72, oxygen isotopic compositions were measured for the Type C (Figs. 3a-c) and Type B-like (Figs. 3d-f) portions. Spongy pyroxene and melilite in the Type C portion show similar ranges of oxygen isotopic compositions ($\Delta^{17}\text{O} = -13\text{‰}$ to -6‰ ; Fig. 10). Fine-grained anorthite shows a wider compositional range ($\Delta^{17}\text{O} = -14\text{‰}$ to -1‰), but most analyses are contaminated by small interstitial grains of Al,Ti-diopside (Fig. 3a). Four clean analyses of anorthite have a narrower compositional range ($\Delta^{17}\text{O} = -8\text{‰}$ to -1‰), with the most ^{16}O -depleted composition (spot 32, Table 1) observed near the CAI periphery (Fig. 3c) where anorthite is

extensively replaced by nepheline and sodalite. In the Type B-like portion, massive Al,Ti-diopside grains are less ^{16}O -rich ($\Delta^{17}\text{O} = -14\text{‰}$ to -6‰) than spinel ($\Delta^{17}\text{O} = -23\text{‰}$). The entire compositional range of Al,Ti-diopside is due to three analyses collected by the CNRS/CRPG ion probe which are contaminated by melilite and spinel (Fig. 3d). Three analyses of Al,Ti-diopside collected at UH are free of inclusions of other minerals (Fig. 3e) and show a much narrower compositional range ($\Delta^{17}\text{O} = -13\text{‰}$ to -12‰), which can be considered as representative of the pyroxene in 6-1-72. Oxygen isotopic analyses of melilite, contaminated to varying degrees by grossular and monticellite (Fig. 3f), range in composition from -7‰ to -2‰ ($\Delta^{17}\text{O}$); the cleanest analyses of melilite (spot #'s. 19, 20; Fig. 3e) have $\Delta^{17}\text{O} = -7\text{‰}$.

Type C CAIs with massive melilite and Al,Ti-diopside

Owing to the unusual abundance of densely crowded spinel grains throughout the inclusion, all ion probe analyses of minerals in CG5 (Fig. 4) are contaminated by spinel (Table 1, Fig. 11). Melilite+spinel and anorthite+spinel spots are ^{16}O -depleted relative to Al,Ti-diopside +spinel ($\Delta^{17}\text{O} = -12\text{‰}$ to -11‰ , -15‰ to -8‰ , and -23‰ , respectively), indicating that spinel and Al,Ti-diopside are ^{16}O -enriched relative to the other two phases.

Type C CAIs with ferromagnesian igneous rims or enclosed chondrule fragments

The interior of CAI 93 (which is overgrown by a chondrule-like, igneous rim; Fig. 5) contains ^{16}O -rich spinel ($\Delta^{17}\text{O} = -16\text{‰}$), Al,Ti-diopside that is much less ^{16}O -rich ($\Delta^{17}\text{O} = -11\text{‰}$ to -8‰) than the spinel and most CAI clinopyroxene, and ^{16}O -poor anorthite and melilite ($\Delta^{17}\text{O} = -2\text{‰}$ and -1‰ , respectively; Table 1, Fig. 12). The oxygen isotopic composition of augite in the ferromagnesian igneous rim is even more ^{16}O -depleted ($\Delta^{17}\text{O} = -8\text{‰}$ to -5‰) than the Al,Ti-diopside in the host CAI interior.

In CAI fragment ABC (Fig. 6), trapped xenocrysts of olivine and low-Ca pyroxene have ^{16}O -poor compositions ($\Delta^{17}\text{O} = -6\text{‰}$ and -4‰ , respectively; Table 1, Figs. 13a,b). Among the indigenous CAI minerals, spinel and Al,Ti-diopside are moderately ^{16}O -enriched ($\Delta^{17}\text{O}$ down to -16‰). The pyroxene shows a wide compositional range ($\Delta^{17}\text{O} = -16\text{‰}$ to -6‰), and both the highest and the lowest values of $\Delta^{17}\text{O}$ were found in the CAI portion containing relict grains of olivine and low-Ca pyroxene. Chromian spinel ($\Delta^{17}\text{O} = -11\text{‰}$), anorthite ($\Delta^{17}\text{O} = -5\text{‰}$ to -1‰) and melilite ($\Delta^{17}\text{O} = +2\text{‰}$) are ^{16}O -depleted to varying degrees (Table 1, Figs. 12a,b).

In CAI TS26F1 (Fig. 7, spinel ($\Delta^{17}\text{O} = -20\text{‰}$ to -19‰) and anorthite ($\Delta^{17}\text{O} = -3\text{‰}$ to -1‰)

have the lightest and the heaviest O-isotopic compositions, respectively (Table 1, Figs. 13c,d). We note, however, that melilite has not been analyzed in this CAI. Al,Ti-diopside grains show a wide compositional range ($\Delta^{17}\text{O} = -15\text{‰}$ to -3‰); those in the CAI core are ^{16}O -enriched ($\Delta^{17}\text{O} = -15\text{‰}$ to -10‰) compared to those in the CAI mantle ($\Delta^{17}\text{O} = -5\text{‰}$ to -3‰). Trapped xenocrysts of augite and olivine have ^{16}O -poor compositions ($\Delta^{17}\text{O} = -8\text{‰}$ and -1‰ , respectively).

DISCUSSION

Oxygen isotope evidence for the relationship of Type C to other varieties of CAI in CV3 chondrites

Type C CAIs have been less studied than other CAI varieties because they are much rarer. Moreover, they have long been a puzzle because their bulk compositions are less consistent with the predictions of nebular condensation than are those of many other types of CAIs (see discussions by Beckett and Grossman, 1988; MacPherson, 2003; MacPherson and Huss, 2005; Krot et al., 2004; Petaev and Wood, 2005). One of the major goals of this project thus has been to establish the relationship between Type Cs vs. other CAI varieties.

The results presented herein demonstrate that Allende Type C CAIs preserve a ^{16}O -rich isotopic signature in some of their primary, high-temperature minerals, especially spinel and Al,Ti-diopside. This pattern is analogous to what is observed in other Allende CAIs such as Types A and B inclusions, and demonstrates that the Type C CAIs are directly related to the other CAIs. Furthermore, the internal isotopic heterogeneity within each individual CAI indicates that the Type Cs, like Types A and B inclusions in CV3 meteorites, must have undergone subsequent complex processing that resulted in partial isotopic exchange with a ^{16}O -depleted reservoir. In this respect all of the CV3 inclusions differ from the majority of CAIs in more primitive chondrites where typically all phases uniformly are ^{16}O -rich ($\Delta^{17}\text{O} \leq -20\text{‰}$; e.g., Aléon et al., 2002; Itoh et al., 2004; Fagan et al., 2007a).

What sets at least some of the Allende Type C CAIs apart from their Types A and B counterparts is that the internal oxygen isotopic heterogeneity is not due exclusively to gas-solid exchange with an external reservoir but, in addition, assimilation of bulk ferromagnesian dust during melting or remelting, possibly in the chondrule-forming region (Krot et al., 2007a,b). This is most clearly evident in *TS26F1*, where the degree of melting and mixing with chondrule material appears to decrease inward, towards the CAI core, as indicated by the differences in

chemical compositions of the core and mantle pyroxenes (Fig. 3 in Krot et al., 2007a) and by a distinct boundary between the finer-grained mantle and the coarser-grained core clearly visible in transmitted light (Fig. 5EA) and the Si K α X-ray map (Fig. 7b in Krot et al., 2007a). Spinel and Al,Ti-diopside grains in the mantle of *TS26F1* are ^{16}O -depleted to varying degrees ($\Delta^{17}\text{O}$ range from -16‰ to -3‰) (Table 1, Figs. 13c,d), from which we infer that those phases experienced oxygen isotopic exchange with the assimilated material. Spinel in the core of *TS26F1* retains an ^{16}O -rich composition ($\Delta^{17}\text{O} = -20\text{‰}$). Although coarse Al,Ti-diopside grains in the CAI core are less ^{16}O -rich than the spinel ($\Delta^{17}\text{O} = -15\text{‰}$ to -10‰), they still are ^{16}O -enriched relative to the pyroxene in the CAI mantle ($\Delta^{17}\text{O} = -5\text{‰}$ to -3‰ ; Figs. 13c,d). These observations imply that spinel in the CAI core is largely relict (i.e., escaped melting during formation of the igneous mantle), whereas Al,Ti-diopside experienced variable degrees of melting and isotopic exchange during the event that produced the mantle or prior to it. In contrast to *TS26F1*, the CAIs *ABC* and *93* experienced higher degrees of remelting. This conclusion is based on the oscillatory zoning of Al,Ti-diopside crystals in *ABC* and *93* (Fig. 11 in Krot et al., 2007a), and the enrichment in Cr_2O_3 and depletion in TiO_2 and Al_2O_3 relative to pyroxenes in typical Type B and Type C CAIs (Fig. 3 in Krot et al., 2007a).

Coarse-grained, lath-shaped anorthite in *93* (Fig. 5), *ABC* (Fig. 6) and *TS26F1* (Fig. 7) is ^{16}O -depleted relative to pyroxene (Figs. 12, 13), which crystallized later. We infer that the ^{16}O -poor compositions of anorthite in these CAIs resulted from postcrystallization isotopic exchange with an ^{16}O -poor reservoir. The oxygen isotopic composition of melilite in these CAIs is similar to that of anorthite, suggesting that melilite also could have experienced isotopic exchange during the same process. The possible nature of this exchange is discussed below.

Oxygen isotopic heterogeneity in Type C CAIs: Implications for the nature of the isotopic exchange process in all CV3 CAIs

One of the more enduring unsolved problems regarding CV3 CAIs is the origin of the internal oxygen isotopic heterogeneities within individual CAIs. The consistent pattern of spinel being more ^{16}O -rich than pyroxene, which in turn is far more ^{16}O -rich than either melilite or anorthite, was originally interpreted (Clayton et al., 1977) as being due to post-solidification exchange between the solid CAI phases and an external reservoir (gas or liquid). The key assumption in that interpretation was that oxygen diffusion in spinel is much slower than in pyroxene, and slower in pyroxene than in melilite or anorthite. However, the validity of that

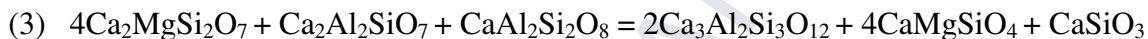
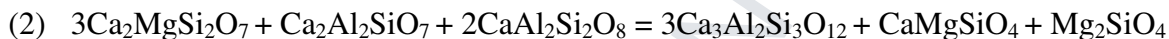
assumption was subsequently called into question by the experiments of Ryerson and McKeegan (1994), who measured the diffusion coefficients of oxygen in spinel, pyroxene, melilite, and anorthite. Using the measured coefficients together with reasonable estimates of grain size and thermal histories, those authors calculated that simple gas-solid exchange cannot easily explain the observed order of ^{16}O -enrichment in natural CAI minerals. The closest (but far from perfect) approach to the natural observations was a model that involved partial melting and subsequent crystallization of an originally ^{16}O -rich CAI in a ^{16}O -depleted gas. In this model, the degree of ^{16}O -enrichment is a function of the degree of melting and igneous crystallization sequence of the CAI. For partial melting of a Type B CAI (the case investigated by Ryerson and McKeegan), spinel is expected to be largely relict from melting and hence should preserve its ^{16}O -rich composition. The subsequent crystallization sequence is melilite (which should be less ^{16}O -rich than the spinel) and then pyroxene + anorthite (both of which should be ^{16}O -poor, and whose relative order is a function of cooling rate). As Ryerson and McKeegan (1994) noted, the model works reasonably well for the spinel, melilite, and anorthite, but fails to explain the observed compositions of Type B pyroxenes. Nonetheless, Ryerson and McKeegan (1994) advocated some variant of this partial melting / fractional crystallization model (coupled perhaps with multiple alteration and melting cycles of the kind proposed by MacPherson and Davis (1993) for one Type B CAI is most likely to be the correct one.

Type C CAIs provide a natural laboratory for testing the partial melting model, because the igneous crystallization sequence of a Type C CAI (see Tronche et al., 2007) is very different from the above: spinel, anorthite, and melilite + pyroxene (whose relative order in this case is a function of bulk composition). The Type C oxygen isotope data presented in this paper in fact refute the partial melting model altogether. Anorthite, which precedes pyroxene in the crystallization sequence, is consistently ^{16}O -poor relative to the pyroxene. The relative isotopic compositions of the phases in the Type Cs is essentially the same as in the Type Bs despite the large differences in igneous crystallization sequences, and we conclude that the partial melting model / fractional crystallization advocated by Ryerson and McKeegan (1994) cannot explain the isotopic heterogeneity within individual Type B or Type C CAIs.

Postcrystallization oxygen isotopic exchange in the Allende Type C CAIs: When and Where?

The oxygen isotopic compositions of secondary monticellite ($\Delta^{17}\text{O} = -2\text{‰}$), forsterite ($\Delta^{17}\text{O} = -5\text{‰}$ to -3‰) and grossular ($\Delta^{17}\text{O} = -9\text{‰}$) that replace spongy melilite in CAI 100 are within analytical uncertainty of (forsterite, monticellite) or slightly ^{16}O -enriched (grossular) relative to those of the melilite itself ($\Delta^{17}\text{O} = -6\text{‰}$). These isotopic compositions likely reflect those of the spongy melilite at the time of replacement, especially in the case of forsterite for which both experiments (Ryerson et al., 1989) and natural observations indicate that oxygen diffusion is very slow. The grossular + monticellite \pm forsterite intergrowths in CAI 160 are distinctly ^{16}O -enriched relative to the melilite they replace (Fig. 8), indicating that oxygen isotopic exchange in CAI 160 melilite continued after formation of the secondary phases.

Pseudomorphic replacement of melilite ($\text{Ca}_2\text{MgSi}_2\text{O}_7$ – $\text{Ca}_2\text{Al}_2\text{SiO}_7$ solid solution) + anorthite ($\text{CaAl}_2\text{Si}_2\text{O}_8$) by grossular ($\text{Ca}_3\text{Al}_2\text{Si}_3\text{O}_{12}$) + monticellite (CaMgSiO_4) \pm forsterite (Mg_2SiO_4) \pm wollastonite (CaSiO_3) can be described by the following closed-system reactions:



Thermodynamic analysis suggests that, under equilibrium conditions for melilite of Åk_{50-70} (covering nearly the entire range of melilite compositions in CAI 160), these reactions occur at $T \leq 750^\circ\text{C}$ (Hutcheon and Newton, 1981; Krot et al., 2007b). However, the common presence of unaltered melilite-anorthite intergrowths in the Allende Type C CAIs 100, 160 and 6-1-72 indicates lack of equilibrium. As a result, the above reactions can only be used to constrain an upper temperature limit for the replacement (note also that the above reactions may not apply at all to vein occurrences of the same phases, where an open system likely prevailed). Finally, grossular itself is not stable above 750°C ; this is much lower than the crystallization temperature of melilite from melts of CAI composition (e.g., Stolper, 1982; Mendybaev et al., 2006), so melting as a mechanism for oxygen isotopic exchange in melilite after formation of grossular can be excluded. Gas-solid exchange is required.

The setting for this exchange is highly debated, and both nebular (e.g., Hutcheon and Newton, 1981; Kimura and Ikeda, 1998; MacPherson, 2003; Fagan et al., 2005, 2006, 2007b; Ushikubo et al., 2006) and asteroidal (Krot et al., 2007b) heating have been proposed to explain formation of grossular in CV chondrites. Both models have problems.

One argument commonly made in favor of an asteroidal setting for the exchange is the general absence of resolved excess ^{26}Mg in secondary phases such as grossular and nepheline,

implying that these phases formed at least 2-3 my (several half-lives of ^{26}Al) after formation of the primary CAI phases (e.g., Krot et al., 1998). However, this observation is not universal. Resolved excesses of ^{26}Mg have been reported for several grossular-anorthite and grossular-melilite intergrowths from Allende CAIs, leading to estimated initial $^{26}\text{Al}/^{27}\text{Al}$ ratios as high as $(1-5)\times 10^{-5}$ (Hutcheon and Newton, 1981; Fagan et al., 2005, 2006, 2007b; Ushikubo et al., 2006). Such high initial $^{26}\text{Al}/^{27}\text{Al}$ ratios imply early formation of grossular, consistent with a nebular setting. It can be argued that, since grossular replaces melilite and anorthite, some or all of its $^{26}\text{Mg}^*$ could be inherited from these minerals (depending on the time of replacement). In cases where only one or two grossular analyses have resolved $^{26}\text{Mg}^*$, fitting a line between the grossular and the origin may result in the erroneous conclusion that elevated levels of live ^{26}Al existed in the grossular at the time of its formation when, in fact, little or none did. However, Fagan et al. (2007b) obtained multiple analyses of grossular within a single CAI, covering a range of Al/Mg ratios, and regression of the grossular analyses alone indicated an initial $^{26}\text{Al}/^{27}\text{Al}$ ratio close to 5×10^{-5} . In our opinion, the cumulative data suggest that grossular at least may have formed via multiple mechanisms covering an extended period of time, possibly in different settings. More work clearly is needed to firmly establish the existence of early-formed (nebular) grossular.

Independent of whether some grossular did form in a nebular setting, there is good reason to think that other grossular formed in an asteroidal setting. Some measured grossular does not contain excess ^{26}Mg , implying late formation, and coarse grain sizes up to $25\ \mu\text{m}$ may require prolonged heating events that are difficult to reconcile with a nebular setting. At the same time, it is generally accepted that Allende experienced thermal metamorphism at temperatures $\geq 350^\circ\text{C}$ (e.g., Bonal et al., 2006 and references therein). The common presence of secondary grossular in CAIs and chondrules from Allende and its virtual absence in CAIs and chondrules from the less metamorphosed CV chondrites Efremovka, Leoville and Kaba (Kimura and Ikeda, 1998; Krot et al., 1998 and references therein; Bonal et al., 2006) are consistent with asteroidal formation of grossular. Finally, given the argument made above that melilite in at least some inclusions (e.g., CAI 160) continued to exchange its oxygen isotopes after formation of the secondary minerals that replace it (grossular, monticellite, forsterite), then we must conclude that the isotopic exchange of the melilite itself (and anorthite?) occurred in an asteroidal setting.

Oxygen isotopic exchange during anhydrous thermal metamorphism is expected to be sluggish (Ryerson and McKeegan, 1994), so it is reasonable to think that oxygen isotopic re-

equilibration in Allende CAIs occurred during fluid-assisted metamorphism (e.g., Ash et al., 1999; Young et al., 1999; Jabeen et al., 1998a, 1998b, 1999; Ash and Young, 2000; Krot et al., 1998, 2006). The composition of this fluid can be inferred from secondary minerals directly precipitated from aqueous/hydrothermal solutions (fayalite, hedenbergite, andradite) and magnetite that formed by oxidation of Fe,Ni-metal (Fig. 14; Choi et al., 2000; Cosarinsky et al., 2002, 2003; Hua et al., 2005; Krot et al., 2006 and references therein). The $\Delta^{17}\text{O}$ values of these secondary minerals (-3‰ to 0‰) in fact are similar to compositions of the melilite we have measured from the Allende Type C CAIs (Figs. 8-13). If our hypothesis regarding fluid-assisted isotopic exchange is correct, melilite and anorthite grains in CAIs from less metamorphosed CV chondrites should be ^{16}O -enriched relative to those same phases in Allende CAIs. The common presence of ^{16}O -rich ($\Delta^{17}\text{O}$ up to -25‰) melilite in Type A CAIs from the CV3.1 Kaba appears to support this hypothesis (Nagashima et al., 2007). Experimental studies of oxygen isotopic exchange between water vapor and melilite are needed to test this hypothesis.

CONCLUSIONS

1. Type C CAIs from Allende originally solidified as ^{16}O -rich melts in a ^{16}O -rich nebular gas, similar to their Types A and B counterparts.
2. At least three Type C CAIs (*ABC*, *TS26F1* and *93*) experienced partial remelting in a ^{16}O -poor gas at the time and place where chondrules were actively forming, trapping and partially assimilating chondrule material within them and also partially exchanging oxygen isotopes of the CAI melts with a surrounding nebular gas.
3. Pyroxene in all Type C CAIs is consistently ^{16}O -rich relative to anorthite, yet in the igneous crystallization sequence for these objects the feldspar always precedes the pyroxene. This fact disproves models for the internal isotopic heterogeneity within individual CAIs in which originally ^{16}O -rich CAIs were partially remelted in a ^{16}O -poor gas, and exchanged isotopes with that gas to a degree that reflected the order of the crystallizing phases. That original model (Ryerson and McKeegan, 1994) was based on Type B CAIs in which pyroxene precedes anorthite in the igneous crystallization sequence, and it clearly does not work for the Type Cs.
4. Grossular-monticellite intergrowths in one CAI (*160*) are ^{16}O -enriched relative to the melilite+anorthite they replace, suggesting the oxygen isotopic exchange of melilite and

anorthite in Type C CAIs continued after formation of grossular. Because pseudomorphic replacement of spongy melilite by grossular and monticellite occurred below 750°C, it is likely that this exchange occurred on the Allende parent body, possibly during fluid-assisted thermal metamorphism. Similar process could have affected melilite and anorthite in other CV CAIs as well as melilite and anorthite in CAIs from metamorphosed CO chondrites.

Acknowledgements: This work was supported by NASA grants NAG5-10610 (A. N. Krot, P.I.), NAG5-11591 (K. Keil, P.I.), NAG5-10468 (G. J. MacPherson, P.I.), and NNH04AB471 (I. D. Hutcheon, P.I.) and Monkasho grants (H. Yurimoto, P.I.). We thank L. Grossman for providing sample of CAIs CG-5 and 6-1-72. We thank Drs. M. Cosarinsky, M. Kimura, R. Ash and S. S. Russell (AE) for detailed reviews and suggestions which helped to focus the paper. This work was performed under the auspices of the U.S. Department Energy by the University of California, Lawrence Livermore National Laboratory under Contract No. W-7405-Eng-48. This is School of Ocean and Earth Science and Technology publications number XXXX and Hawai'i Institute of Geophysics and Planetology publication number XXXX.

REFERENCES

- Aléon J., Krot A. N., and McKeegan K. D. (2002) Ca-Al-rich inclusions and amoeboid olivine aggregates from the CR carbonaceous chondrites. *Meteorit. Planet. Sci.* **37**, 1729-1755.
- Aléon J., Krot A. N., McKeegan K. D., MacPherson G. J., and Ulyanov A. A. (2005a) Fine-grained, spinel-rich inclusions from the reduced CV chondrite Efremovka: II. Oxygen isotopic compositions. *Meteorit. Planet. Sci.* **40**, 1043-1058.
- Aléon J., El Goresy A., and Zinner E. (2005b) First evidence for co-existing ^{16}O -poor and ^{16}O -rich gases in the early solar nebula inferred from a compound Ca-Al-rich inclusion from Efremovka (abstract). In Workshop on *Oxygen in the Earliest Solar System*, Gatlinburg, Tennessee, LPI Contribution No. 1278, 8.
- Amelin Y., Krot A. N., Hutcheon I. D., and Ulyanov A. A. (2002) Pb isotopic ages of chondrules and Ca,Al-rich inclusions. *Science* **297**, 1678-1683.
- Ash R. D., Young E. D., Rumble III D., Alexander C. M. O'D., and MacPherson G. J. (1999) Oxygen isotope systematics in Allende chondrules (abstract). *Lunar Planet. Sci.* **XXX**, #1836.

- Ash R. D. and Young E. D. (2000) Clarity and confusion: The history of Allende chondrules as evinced by oxygen isotopes (abstract). *Lunar Planet. Sci.* **XXX**, #1881.
- Beckett J. R. and Grossman L. (1988) The origin of Type C inclusions from carbonaceous chondrites. *Earth Planet. Sci. Lett.* **89**, 1-14.
- Bonal L., Quirico E., Bourot-Denise M., and Montagnac G. (2006) Determination of the petrologic type of CV3 chondrites by Raman spectroscopy of included organic matter. *Geochim. Cosmochim. Acta* **70**, 1849-1863.
- Choi B.-G., Krot A. N., and Wasson J. T. (2000) Oxygen-isotopes in magnetite and fayalite in CV chondrites Kaba and Mokoia. *Meteorit. Planet. Sci.* **35**, 1239-1248.
- Clayton R. N., Onuma N., Grossman L., and Mayeda T. K. (1977) Distribution of the pre-solar component in Allende and other carbonaceous chondrites. *Earth Planet. Sci. Lett.* **304**, 209-224.
- Cosarinsky M., Leshin L. A., MacPherson G. J., Krot A. N., and Guan Y. (2002) Oxygen isotopic composition of olivines from matrices and accretionary rims around Ca-Al-rich inclusions in CV chondrites (abstract). *Meteorit. Planet. Sci.* **37 (Suppl.)**, A38.
- Cosarinsky M., Leshin L. A., MacPherson G. J., Krot A. N., and Guan Y. (2003) Oxygen isotope composition of Ca-Fe-rich silicates in and around an Allende Ca-Al-rich inclusion (abstract). *Lunar Planet. Sci.* **XXXIV**, #1043.
- Fagan T. J., Krot A. N., Keil K., and Yurimoto H. (2004) Nebular setting of oxygen isotopic alteration in a coarse-grained Ca-Al-rich inclusion from Efremovka. *Meteorit. Planet. Sci.* **39**, 1257-1272.
- Fagan T. J., Guan Y., MacPherson G. J., and Huss G. R. (2005) Al-Mg isotopic evidence for separate nebular and parent body alteration events in two Allende CAIs (abstract). *Lunar Planet. Sci.* **XXXVI**, #1820.
- Fagan T. J., Guan Y., and MacPherson G. J. (2006) Al-Mg isotopic constraints on alteration of Allende Ca-Al-rich inclusions (abstract). *Lunar Planet. Sci.* **XXXVII**, #1213.
- Fagan T. J., Krot A. N., Kobayashi S., and Yurimoto H. (2007a) Correlation between texture and oxygen isotopic systematics in CAIs from Acfer 094 (abstract). *Lunar Planet. Sci.* **XXXVIII**, #1252.
- Fagan T. J., Guan Y., and MacPherson G. J. (2007b) Al-Mg isotopic evidence for episodic alteration of Ca-Al-rich inclusions from Allende. *Meteorit. Planet. Sci.* **42**, 1221-1240.
- Greenwood J. P. (2004) Disequilibrium melting of refractory inclusions: A mechanism for high-

- temperature oxygen isotope exchange in the solar nebula (abstract). *Lunar Planet. Sci.* **XXXV**, #2132.
- Grossman L. and Ganapathy R. (1975) Volatile elements in Allende inclusions. *Proc. Lunar Sci. Conf. 6th, Geochim. Cosmochim. Acta Supplement* **6**, 1729-1736.
- Gurenko A. A. and Chaussidon M. (2002) Oxygen isotopic variations in primitive tholeiites of Iceland: evidence from a SIMS study of glass inclusions, olivine phenocrysts and pillow rim glasses. *Earth Planet. Sci. Lett.* **205**, 63-79.
- Harazono K. and Yurimoto H. (2003) Oxygen isotopic variations in a fluffy Type A CAI from the Vigarano meteorite (abstract). *Lunar Planet. Sci.* **XXXIV**, #1540.
- Hiyagon H. and Hashimoto A. (1999) ^{16}O excesses in olivine inclusions in Yamato-86009 and Murchison chondrites and their relation to CAIs. *Science*, **283**, 828-830.
- Hua X., Huss G. R., Tachibana S., and Sharp T. G. (2005) Oxygen, silicon, and Mn-Cr isotopes of fayalite in the Kaba oxidized CV3 chondrite: Constraints for its formation history. *Geochim. Cosmochim. Acta* **69**, 1333-1348.
- Huss G. R., MacPherson G. J., Wasserburg G. J., Russell S. S., and Srinivasan G. (2001) ^{26}Al in CAIs and Al-chondrules from unequilibrated ordinary chondrites. *Meteorit. Planet. Sci.* **36**, 975-997.
- Hutcheon I. D. and Newton R. C. (1981) Mg isotopes, mineralogy, and mode of formation of secondary phases in C3 refractory inclusions (abstract). *Lunar. Planet. Sci.* **XII**, 491-493.
- Imai H. and Yurimoto H. (2000) Oxygen and magnesium isotopic distributions in a Type C CAI from the Allende meteorite (abstract). *Lunar Planet. Sci.* **XXXI**, #1510.
- Ito M., Nagasawa H., and Yurimoto H. (2004) Oxygen isotopic SIMS analysis in Allende CAI: details of the very early thermal history of the solar system. *Geochim. Cosmochim. Acta* **68**, 2905-2923.
- Itoh S., Kojima H., and Yurimoto H. (2004) Petrography and oxygen isotopic compositions in refractory inclusions from CO chondrites. *Geochim. Cosmochim. Acta* **68**, 183-194.
- Jabeen I., Kusakabe M., Nakamura T., and Nagao K. (1998a) Oxygen isotopic signature in Allende chondrules (abstract). *Meteorit. Planet. Sci.* **33** (Suppl.), A76-A77.
- Jabeen I., Kusakabe M., Nakamura T., and Nagao K. (1998b) Oxygen isotope study of Tsukuba chondrite, some HED meteorites and Allende chondrules. *Antarct. Meteorite Res.* **11**, 122-135.
- Jabeen I., Kusakabe M., Nakamura T., and Nagao K. (1999) Parent body processes in Allende:

- Evidence from oxygen isotope study of the Allende chondrules (abstract). *Symp. Antarct. Meteorit.* **24**, 59-61.
- Kim G. L., Yurimoto H., and Sueno S. (2002) Oxygen isotopic composition of a compound Ca-Al-rich inclusion from Allende meteorite: Implications for origin of palisade bodies and O-isotopic environment in the CAI-forming region. *J. Mineral. Petrol. Sci.* **97**, 161-167.
- Kimura M. and Ikeda Y. (1998) Hydrous and anhydrous alterations of chondrules in Kaba and Mokoia CV chondrites. *Meteorit. Planet. Sci.* **33**, 1139-1146.
- Kita N. T., Huss G. R., Tachibana S., Amelin Y., Nyquist L. E., and Hutcheon I. D. (2005) Constraints on the origin of chondrules and CAIs from short-lived and long-lived radionuclides. In *Chondrules and the Protoplanetary Disk*, eds. Krot A. N., Scott E. R. D., and Reipurth B., Astronomical Society of the Pacific Conference Series **341**, 558-588.
- Kita N. T., Ushikubo T., Fu B., Spicuzza M. J., and Valley J. W. (2007) Analytical developments on oxygen three isotope analyses using a new generation ion microprobe IMS-1280 (abstract). *Lunar Planet. Sci.* **XXXVIII**, #1981.
- Krot A. N., Petaev M. I., Scott E. R. D., Choi B.-G., Zolensky M. E., and Keil K. (1998) Progressive alteration in CV3 chondrites: More evidence for asteroidal alteration. *Meteorit. Planet. Sci.* **33**, 1065-1085.
- Krot A. N., McKeegan K. D., Leshin L. A., MacPherson G. J., and Scott E. R. D. (2002) Existence of an ^{16}O -rich gaseous reservoir in the solar nebula. *Science* **295**, 1051-1054.
- Krot A. N., MacPherson G. J., Ulyanov A. A. and Petaev M. I. (2004) Fine-grained, spinel-rich inclusions from the reduced CV chondrites Efremovka and Leoville: I. Mineralogy, petrology and bulk chemistry. *Meteoritics and Planetary Science* **39**, 1517-1553
- Krot A. N., Hutcheon I. D., Yurimoto H., Cuzzi J. N., McKeegan K. D., Scott E. R. D., Libourel G., Chaussidon M., Aléon J., and Petaev M. I. (2005a) Evolution of oxygen isotopic composition in the inner solar nebula. *Astrophys. J.* **622**, 1333-1342.
- Krot A. N., Yurimoto H., Hutcheon I. D., and MacPherson G. J. (2005b) Relative chronology of CAI and chondrule formation: Evidence from chondrule-bearing igneous CAIs. *Nature* **434**, 998-1001.
- Krot A. N., Yurimoto H., Hutcheon I. D., MacPherson G. J., and Paque J. (2007a) Remelting of refractory inclusions in the chondrule-forming regions: Evidence from the chondrule-bearing Type C calcium-aluminum-rich inclusions from Allende. *Meteorit. Planet. Sci.*, in press.

- Krot A. N., Yurimoto H., Hutcheon I. D., Libourel G., Chaussidon M., Petaev M. I., MacPherson G. J., Paque-Heather J., and Wark D. (2007b) Type C CAIs from Allende: Evidence for multistage formation. *Geochim. Cosmochim. Acta*, in press.
- MacPherson G. J. (2003) Calcium-aluminum-rich inclusions in chondritic meteorites. In *Meteorites, Comet And Planets* (ed. A. M. Davis) Vol. 1 *Treatise On Geochemistry* (eds. H. D. Holland and K. K. Turekian), pp. 201-246. Elsevier-Pergamon, Oxford.
- MacPherson G. J. and Davis A. M. (1993) A petrologic and ion microprobe study of a Vigarano type B2 refractory inclusion: Evolution by multiple stages of melting and alteration. *Geochim. Cosmochim. Acta* **57**, 231-243.
- MacPherson G. J., Wark D. A., and Armstrong J. T. (1988) Primitive material surviving in chondrites: Refractory inclusions. In *Meteorites and the Early Solar System* (J. F. Kerridge and M. S. Matthews, eds.), pp. 746-807. Univ. of Arizona Press, Tucson.
- MacPherson G. J., Davis A. M., and Zinner E. K. (1995) The distribution of aluminum-26 in the early solar system: A reappraisal. *Meteoritics* **30**, 365-386.
- MacPherson G. J., and Huss G. R. (2005) Petrogenesis of Al-rich chondrules: Evidence from bulk compositions and phase equilibria. *Geochim. Cosmochim. Acta* **69**, 3099-3127.
- McKeegan K. D., Leshin L. A., and MacPherson G. J. (1998) Oxygen isotopic stratigraphy in a Vigarano type-A calcium-aluminum-rich inclusion (abstract). *Meteorit. Planet. Sci.* **33** (Suppl.), A102-A103.
- Mendybaev R. A., Richter F. M. and Davis A. M. (2006) Crystallization of melilite from CMAS-liquids and the formation of the melilite mantle of Type B1 CAIs: Experimental simulations. *Geochim. Cosmochim. Acta* **70**, 2622-2642.
- Nagashima K., Krot A. N., Huss G. R., and X. Hua (2007) Common presence of ¹⁶O-rich melilite in calcium-aluminum-rich inclusions from the least metamorphosed CV carbonaceous chondrite Kaba (abstract). *Lunar Planet Sci.* **XXXVIII**, #2059.
- Petaev M. I. and Wood J. A. (2005) Meteoritic constraints on temperatures, pressures, cooling rates, chemical compositions, and modes of condensation in the solar nebula. in *Chondrites and the Protoplanetary Disk*, eds. Krot A. N., Scott E. R. D. and Reipurth B. Astronomical Society of the Pacific Conference Series **341**, pp. 373-407.
- Pouchou J. L. and Pichoir F. (1984) A new model for quantitative X-ray microanalysis. I Application to the analysis of homogeneous samples. *La Recherche Aerospatiale*, **3**, 13-38.

- Russell S. S., Srinivasan, G., Huss G. R., Wasserburg G. J. and MacPherson G. J. (1996) Evidence for Widespread ^{26}Al in the Solar Nebula and Constraints for Nebula Timescales. *Science* **273**, 757-762.
- Russell S. S., MacPherson G. J., Leshin L. A., and McKeegan K. D., (2000) ^{16}O enrichments in aluminum-rich chondrules from ordinary chondrites. *Earth Planet. Sci. Lett.* **184**, 57-74
- Ryerson F. J., Durham W. B., Cherniak D. J., and Lanford W.A. (1989) Oxygen diffusion in olivine: Effect of oxygen fugacity and implication for creep. *J. Geophys. Res.* **94**, 4105-4118.
- Ryerson F. J. and McKeegan K. D. (1994) Determination of oxygen self-diffusion in akermanite, anorthite, diopside, and spinel: Implications for oxygen isotopic anomalies and the thermal histories of Ca-Al-rich inclusions. *Geochim. Cosmochim. Acta* **58**, 3713-3734.
- Stolper E. (1982) Crystallization sequences of Ca-Al-rich inclusions from Allende: an experimental study. *Geochim. Cosmochim. Acta* **46**, 2159-2180.
- Stolper E. and Paque J. M. (1986) Crystallization sequences of Ca-Al-rich inclusions from Allende: The effects of cooling rate and maximum temperature. *Geochim. Cosmochim. Acta* **50**, 1785-1806.
- Tronche E. J., Hewins R. H., and MacPherson G. J. (2007) Formation conditions of aluminum-rich chondrules. *Geochim. Cosmochim. Acta* **71**, 3361-3381
- Ushikubo T., Guan Y., Hiyagon H., Sugiura N., and Leshin L. A. (2006) ^{36}Cl , ^{26}Al and oxygen isotopes in an Allende CAI: Implications for secondary alteration in the early solar system (abstract). *Lunar Planet. Sci.* **XXXVII**, #2082.
- Wark D. A. (1987) Plagioclase-rich inclusions in carbonaceous chondrite meteorites: Liquid condensates? *Geochim. Cosmochim. Acta* **51**, 221-242.
- Yoneda S., and Grossman L. (1995) Condensation of CaO-MgO- Al_2O_3 - SiO_2 liquids from cosmic gases. *Geochim. Cosmochim. Acta* **59**, 3413-3444.
- Yoshitake M., Koide Y., and Yurimoto H. (2002) Distributions of oxygen isotopes in Wark-Lovering rim of a Type B2 CAI from the Vigarano meteorite (abstract). *Lunar Planet. Sci.* **XXXIII**, #1502.
- Young E. D., Ash R. D., England P., and Rumble D. (1999) Fluid flow in chondritic parent bodies: Deciphering the compositions of planetesimals. *Science* **286**, 1331-1335.
- Yurimoto H., Morioka M., and Nagasawa H. (1989) Diffusion in single-crystals of melilite: I. Oxygen. *Geochim. Cosmochim. Acta* **53**, 2387-2394.

- Yurimoto H., Ito M., and Nagasawa H. (1998) Oxygen isotope exchange between refractory inclusion in Allende and solar nebula gas. *Science* **282**, 1874-1877.
- Zolotov M. Y., Mironenko M. V., and Shock E. L. (2006) Thermodynamic constraints on fayalite formation on parent bodies of chondrites. *Meteorit. Planet. Sci.* **41**, 1775-1797.

ACCEPTED MANUSCRIPT

Fig. 1. Backscattered electron (BSE) images of a Type C CAI 160. Ion probe spots are numbered; numbers correspond to those listed in Table 1. an = anorthite; di = Al,Ti-diopside; fo = forsterite; grs = grossular; mel = melilite; mnl = monticellite; sp = spinel.

Fig. 2. BSE images of a Type C CAI 100. Ion probe spots are outlined and numbered; numbers correspond to those listed in Table 1. Small and large ellipses correspond to ion probe spots analyzed by the Hokudai and CNRS/CRPG ion microprobes, respectively. an = anorthite; di = Al,Ti-diopside; fo = forsterite; grs = grossular; mel = melilite; mnl = monticellite; sp = spinel.

Fig. 3. BSE of the Type C (a-c) and Type B-like (d-f) portions of a CAI 6-1-72. Ion probe spots are outlined and numbered; numbers correspond to those listed in Table 1. Ellipsoid spots are from the CNRS/CRPG ims-1270; square regions are from the UH ims-1280. an = anorthite; di = Al,Ti-diopside; fo = forsterite; grs = grossular; mel = melilite; mnl = monticellite; sp = spinel.

Fig. 4. BSE images of a Type C CAI CG5. Ion probe spots are outlined and numbered; numbers correspond to those listed in Table 1. an = anorthite; di = Al,Ti-diopside; mel = melilite; sp = spinel.

Fig. 5. (a) Combined elemental maps in Mg (red), Ca (green) and Al (blue) $K\alpha$ X-rays, (b) combined elemental maps in Mg (red), Ti (green) and Al (blue) $K\alpha$ X-rays, and (c-f) BSE images of a Type C 93. Regions outlined and labeled in “a” are shown in detail in “c”, “d”, and “f”. Region outlined in “d” is shown in detail in “e”. Ion probe spots are outlined and numbered; numbers correspond to those listed in Table 1. an = anorthite; aug = augite; di = Al,Ti-diopside; fa = ferrous olivine; grs = grossular; mel = melilite; mnl = monticellite; pg = pigeonite; sod = sodalite.

Fig. 6. (a) Combined elemental maps in Mg (red), Ca (green) and Al (blue) $K\alpha$ X-rays, (b) combined elemental maps in Mg (red), Ti (green) and Al (blue) $K\alpha$ X-rays, and (c-f) BSE images of a Type C ABC. Regions outlined and labeled in “b” are shown in detail in “c-f”. Ion probe spots are outlined and numbered; numbers correspond to those listed in Table 1. an = anorthite; aug = augite; Cr-sp = chromium spinel; di = Al,Ti-diopside; ol = olivine; grs = grossular; lpx = low-Ca pyroxene; mel = melilite; mes = mesostasis; mnl = monticellite; nph = nepheline; pl = anorthitic plagioclase; sf = sulfide; sod = sodalite; sp = spinel; wol = wollastonite.

Fig. 7. Combined elemental maps in Mg (red), Ca (green) and Al (blue) $K\alpha$ X-rays, (b) combined elemental maps in Mg (red), Ti (green) and Al (blue) $K\alpha$ X-rays, and (c, d) BSE images of a Type C TS26. Regions outlined in and labeled “a” are shown in detail in “c” and “d”. Ion probe spots are outlined and numbered; numbers correspond to those listed in Table 1. an = anorthite; aug = augite; di = Al,Ti-diopside; ol = olivine; lpx = low-Ca pyroxene; mel = melilite; sod = sodalite; sp = spinel.

Fig. 8. Oxygen isotopic compositions of a Type C CAI 160. In “a”, data are plotted as $\delta^{17}\text{O}$ vs. $\delta^{18}\text{O}$; to illustrate variations in oxygen isotopic compositions of different minerals, in “b”, the same data, grouped by minerals, are plotted as deviations from the terrestrial fractionation line (TFL), $\Delta^{17}\text{O}$ ($= \delta^{17}\text{O} - 0.52 \times \delta^{18}\text{O}$). Carbonaceous chondrite anhydrous mineral (CCAM) line is shown for reference. an = anorthite; di = Al,Ti-diopside; grs+mnl = grossular + monticellite; mel = melilite; sp = spinel. Data were collected at CNRS/CRPG; error bars are 2σ .

Fig. 9. Oxygen isotopic compositions of a Type C CAI 100 collected using CNRS-CRPG (a, b; 2σ error) and Hokudai (c, d; 2σ error) ion microprobes. In “a” and “b”, data are plotted as $\delta^{17}\text{O}$ vs. $\delta^{18}\text{O}$; in “c” and “d”, the same data, grouped by minerals, are plotted as $\Delta^{17}\text{O}$. an = anorthite; di = Al,Ti-diopside; fo = forsterite; grs = grossular; mel = melilite; mnl = monticellite; sp = spinel.

Fig. 10. Oxygen isotopic compositions of the Type B-like and Type C portions of a CAI 6-1-72. In “a”, data are plotted as $\delta^{17}\text{O}$ vs. $\delta^{18}\text{O}$; to illustrate variations in oxygen isotopic compositions of different minerals, in “b”, the same data, grouped by minerals, are plotted as $\Delta^{17}\text{O}$. an = anorthite; di = Al,Ti-diopside; grs = grossular; mel = melilite; sp = spinel. Legends in the top left corner and the bottom right corner correspond to the data collected with the CNRS/CRPG and UH ion microprobes, respectively; error bars are 2σ .

Fig. 11. Oxygen isotopic compositions of a Type C CAI *CG5*. In “a”, data are plotted as $\delta^{17}\text{O}$ vs. $\delta^{18}\text{O}$; in “b”, the same data are plotted as $\Delta^{17}\text{O}$. an = anorthite; di = Al,Ti-diopside; mel = melilite; sp = spinel. Data were collected at CNRS/CRPG; size of symbols correspond to 2σ errors.

Fig. 12. Oxygen isotopic compositions of a Type C CAI *#93* with a chondrule-like, igneous rim. In “a”, data are plotted as $\delta^{17}\text{O}$ vs. $\delta^{18}\text{O}$; in “b”, the same data, grouped by minerals, are plotted as $\Delta^{17}\text{O}$. an = anorthite; aug = augite; di = Al,Ti-diopside; mel = melilite; sec = secondary minerals; sp = spinel. Data were collected at CNRS/CRPG; error bars are 2σ .

Fig. 13. Oxygen isotopic compositions of Type C CAIs *ABC* (a, b) and *TS26* (c, d) with chondrule fragments in their peripheries (from Krot et al., 2007b). In “a” and “c”, data are plotted as $\delta^{17}\text{O}$ vs. $\delta^{18}\text{O}$; in “b” and “d”, the same data, grouped by minerals, are plotted as $\Delta^{17}\text{O}$. an = anorthite; aug = augite; Cr-sp = Cr-spinel; di = Al,Ti-diopside; lpx = low-Ca pyroxene; mel = melilite; ol = olivine; sp = spinel. Data were collected at Hokudai; error bars are 2σ .

Fig. 14. a, b - Oxygen isotopic compositions of secondary magnetite (Mgt) and fayalite (Fa) in type I chondrules in the oxidized Bali-like CV chondrites Mokoia and Kaba (data from Choi et al., 2000; Hua et al., 2005; the latter are labeled by “*” in the legend to “b”). c, d - Oxygen isotopic compositions of secondary magnetite, Ca,Fe-pyroxenes (CaFe-px) and andradite (Andr) in various Allende components. Data for magnetite from Choi et al. (2000); data for Ca,Fe-pyroxenes, fayalitic olivine and andradite from Krot et al. (2000) and Cosarinsky et al. (2003). Error bars are 2σ .

Fig. 1EA. (a) Combined elemental maps in Mg (red), Ca (green) and Al (blue) $K\alpha$ X-rays and (b) elemental map in Ti $K\alpha$ X-rays of a Type C *160*. an = anorthite; di = Al,Ti-diopside; fgr = fine-grained rim; fsl = ferrosilite; hed = hedenbergite; mel = melilite; mnl = monticellite; nph = nepheline; sod = sodalite; sp = spinel; WLR = Wark-Lovering rim.

Fig. 2EA. Combined elemental maps in Mg (red), Ca (green) and Al (blue) $K\alpha$ X-rays of four fragments of a Type C *100*. an = anorthite; di = Al,Ti-diopside; fo = forsterite; grs = grossular; mel = melilite; mnl = monticellite; nph = nepheline; sp = spinel.

Fig. 3EA. (a) Combined elemental maps in Mg (red), Ca (green) and Al (blue) $K\alpha$ X-rays and (b) elemental map in Ca $K\alpha$ X-rays of a Type C *6-1-72*. an = anorthite; di = Al,Ti-diopside; mel = melilite; nph = nepheline; ol = olivine; sod = sodalite; sp = spinel. The CAI consists of two mineralogically distinct portions – Type B-like and Type C.

Fig. 4EA. (a) Combined elemental maps in Mg (red), Ca (green) and Al (blue) $K\alpha$ X-rays and (b) elemental map in Ti $K\alpha$ X-rays of a Type C *CG5*. an = anorthite; di = Al,Ti-diopside; mel = melilite; sp = spinel.

Fig. 5EA. (a) Optical micrograph in cross-polarized transmitted light and (b) combined elemental maps in Mg (red), Ca (green) and Al (blue) $K\alpha$ X-rays of a Type C *TS26*. Arrows in “b” indicate relict chondrule fragments in the CAI mantle.

Fig. 1. Backscattered electron (BSE) images of a Type C CAI 160. Ion probe spots are numbered; numbers correspond to those listed in Table 1. an = anorthite; di = Al,Ti-diopside; fo = fosterite; grs = grossular; mel = melilite; mnl = monticellite; sp = spinel.

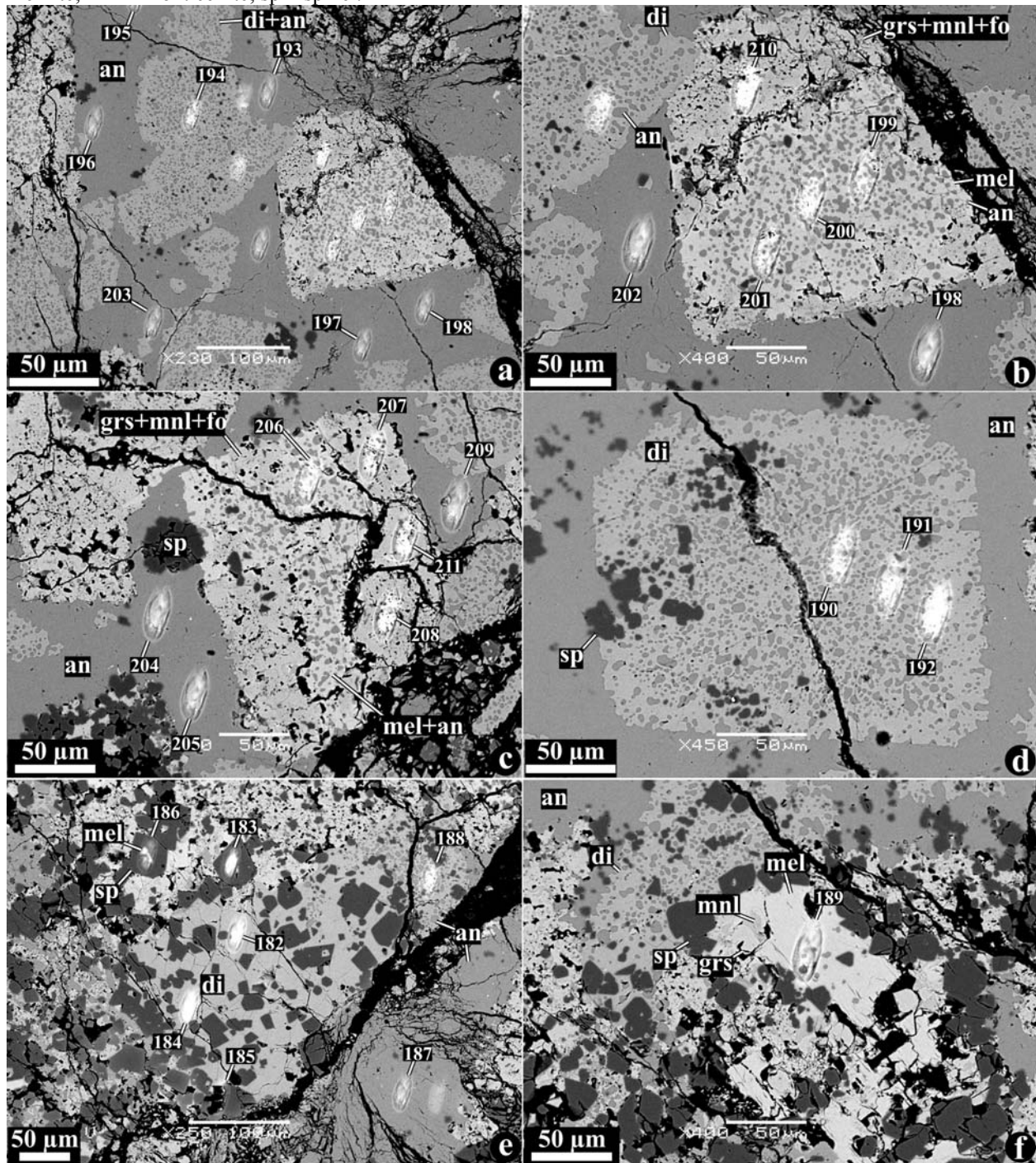


Fig. 2. BSE images of a Type C CAI 100. Ion probe spots are outlined and numbered; numbers correspond to those listed in Table 1. Small and large ellipses correspond to ion probe spots analyzed by the Hokudai and CNRS/CRPG ion microprobes, respectively. an = anorthite; di = Al,Ti-diopside; fo = forsterite; grs = grossular; mel = melilite; mnl = monticellite; sp = spinel.

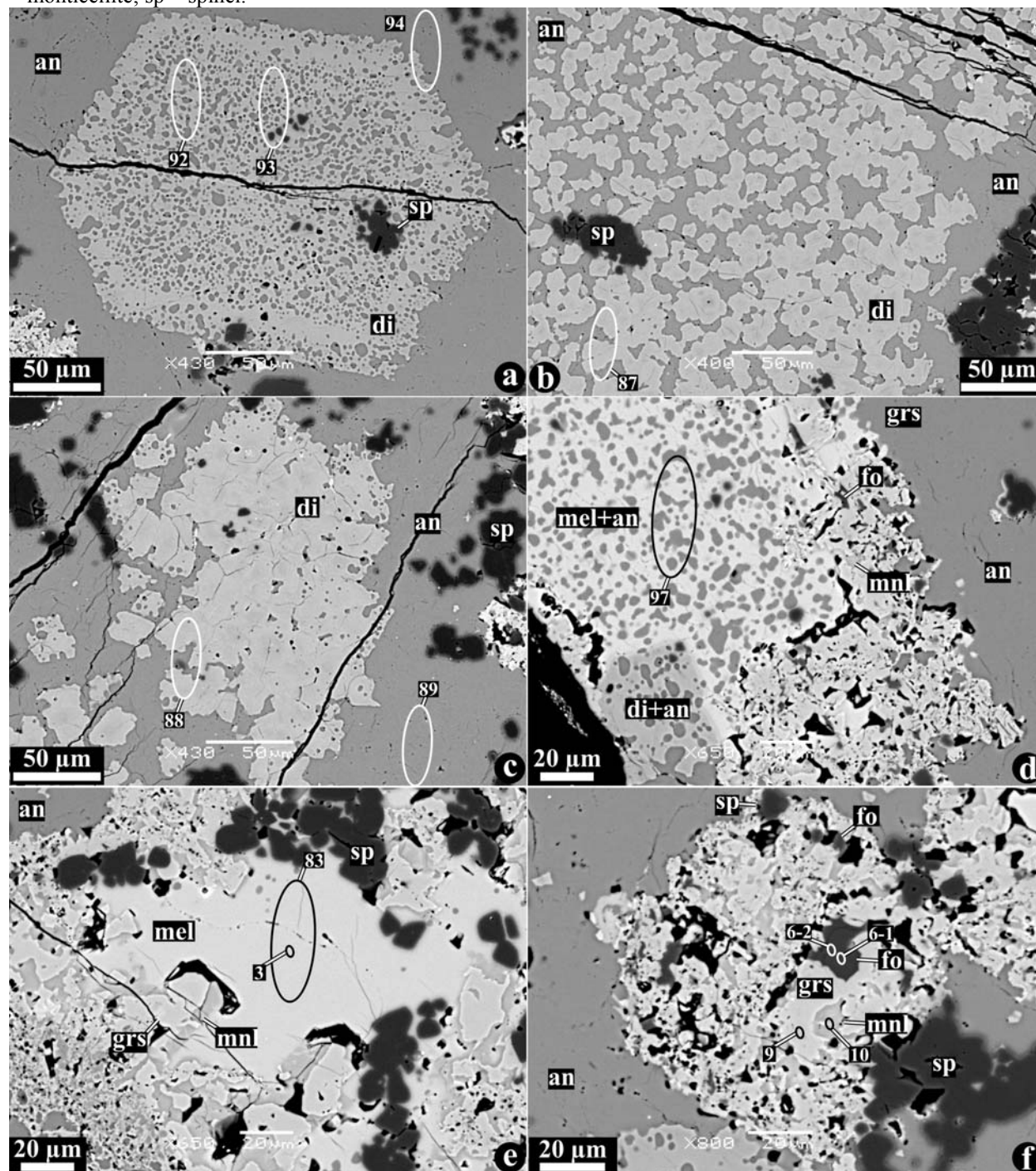


Fig. 3. BSE of the Type C (a-c) and Type B-like (d-f) portions of a CAI 6-1-72. Ion probe spots are outlined and numbered; numbers correspond to those listed in Table 1. Ellipsoid spots are from the CNRS/CRPG ims-1270; square regions are from the UH ims-1280. an = anorthite; di = Al,Ti-diopside; fo = forsterite; grs = grossular; mel = melilite; mnl = monticellite; sp = spinel.

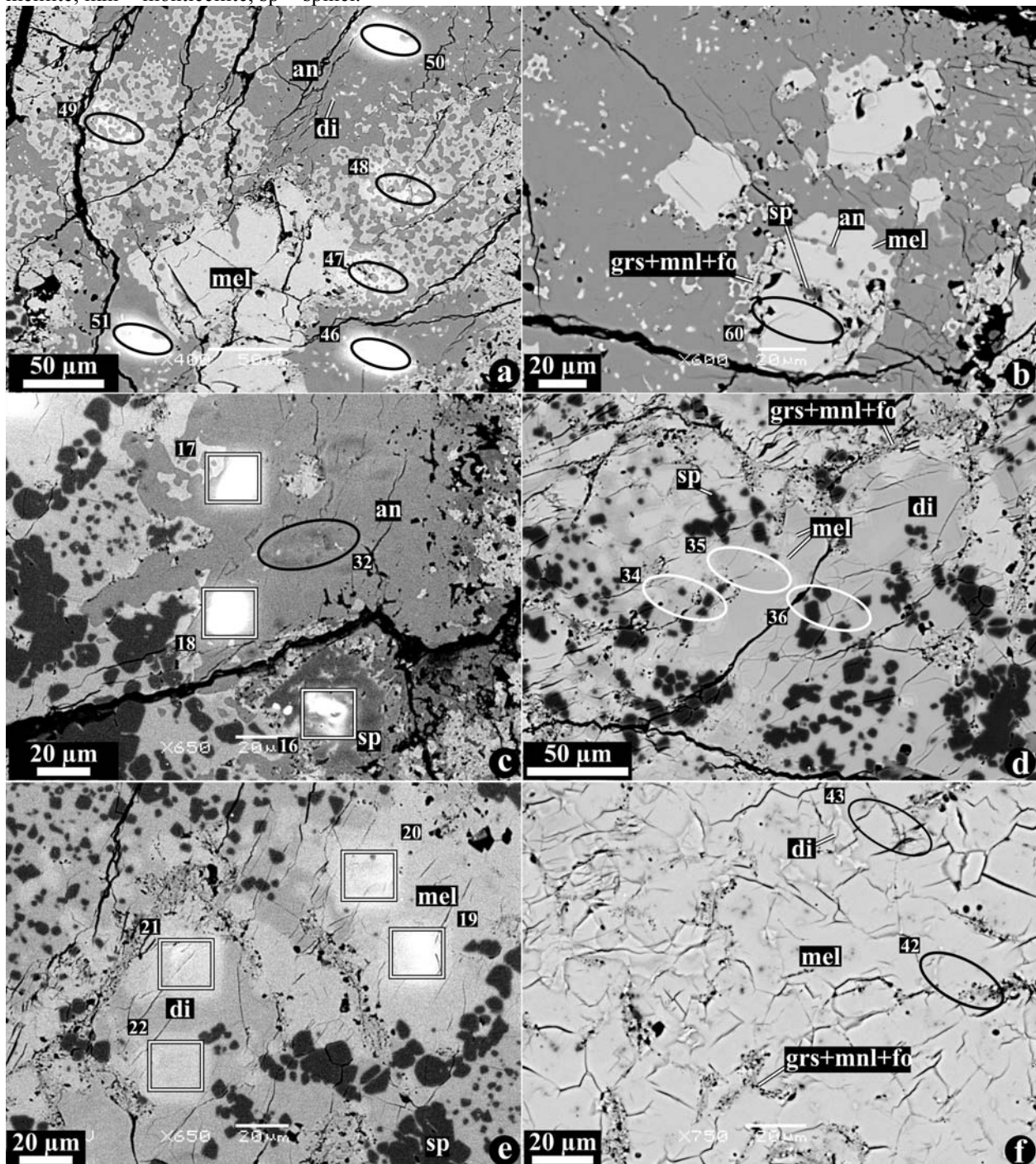


Fig. 4. BSE images of a Type C CAI CG5. Ion probe spots are outlined and numbered; numbers correspond to those listed in Table 1. an = anorthite; di = Al,Ti-diopside; mel = melilite; sp = spinel.

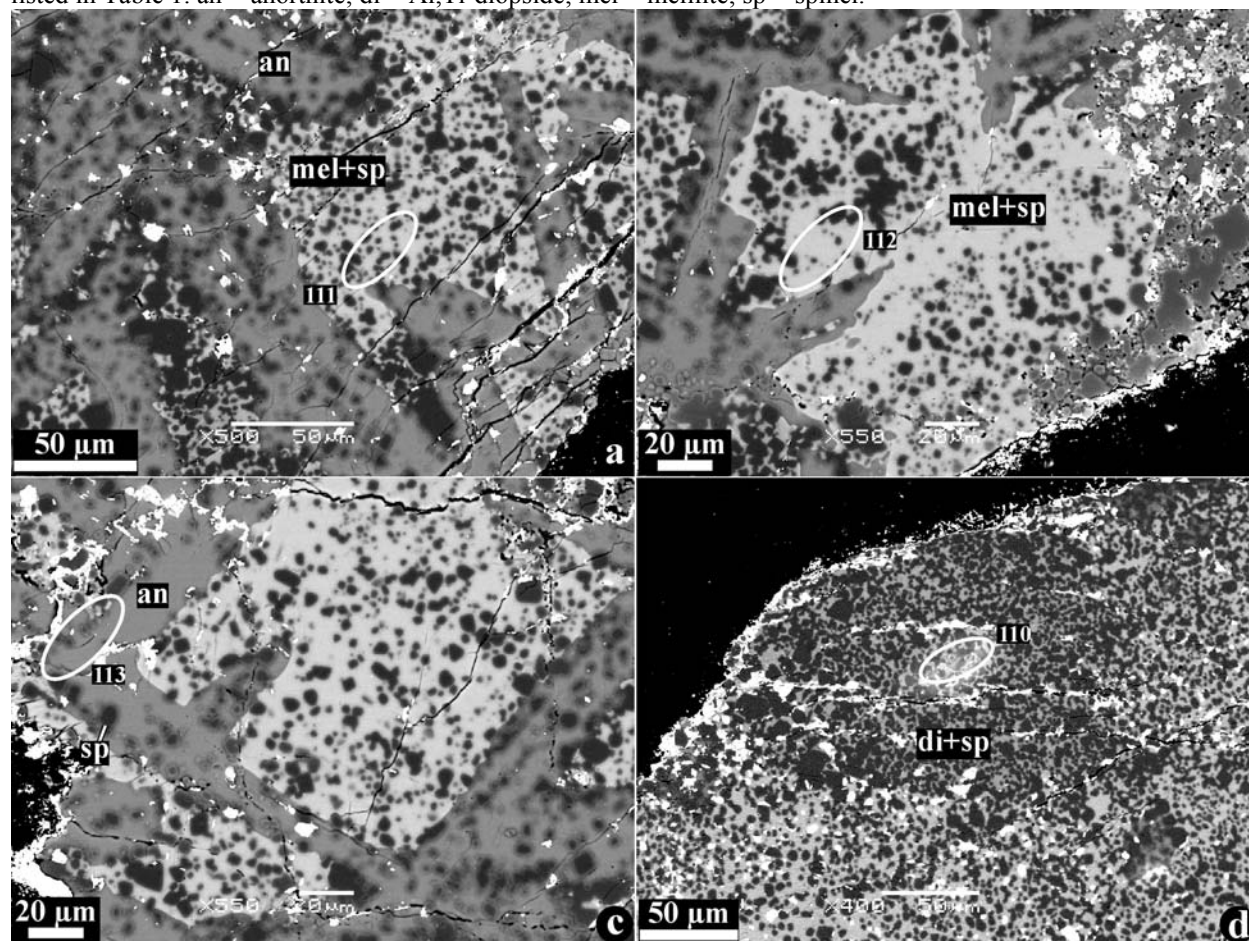


Fig. 5. (a) Combined elemental maps in Mg (red), Ca (green) and Al (blue) $K\alpha$ X-rays, (b) combined elemental maps in Mg (red), Ti (green) and Al (blue) $K\alpha$ X-rays, and (c-f) BSE images of a Type C 93. Regions outlined and labeled in “a” are shown in detail in “c”, “d”, and “f”. Region outlined in “d” is shown in detail in “e”. Ion probe spots are outlined and numbered; numbers correspond to those listed in Table 1. an = anorthite; aug = augite; di = Al,Ti-diopside; fa = ferrous olivine; grs = grossular; mel = melilite; mnl = monticellite; pg = pigeonite; sod = sodalite.

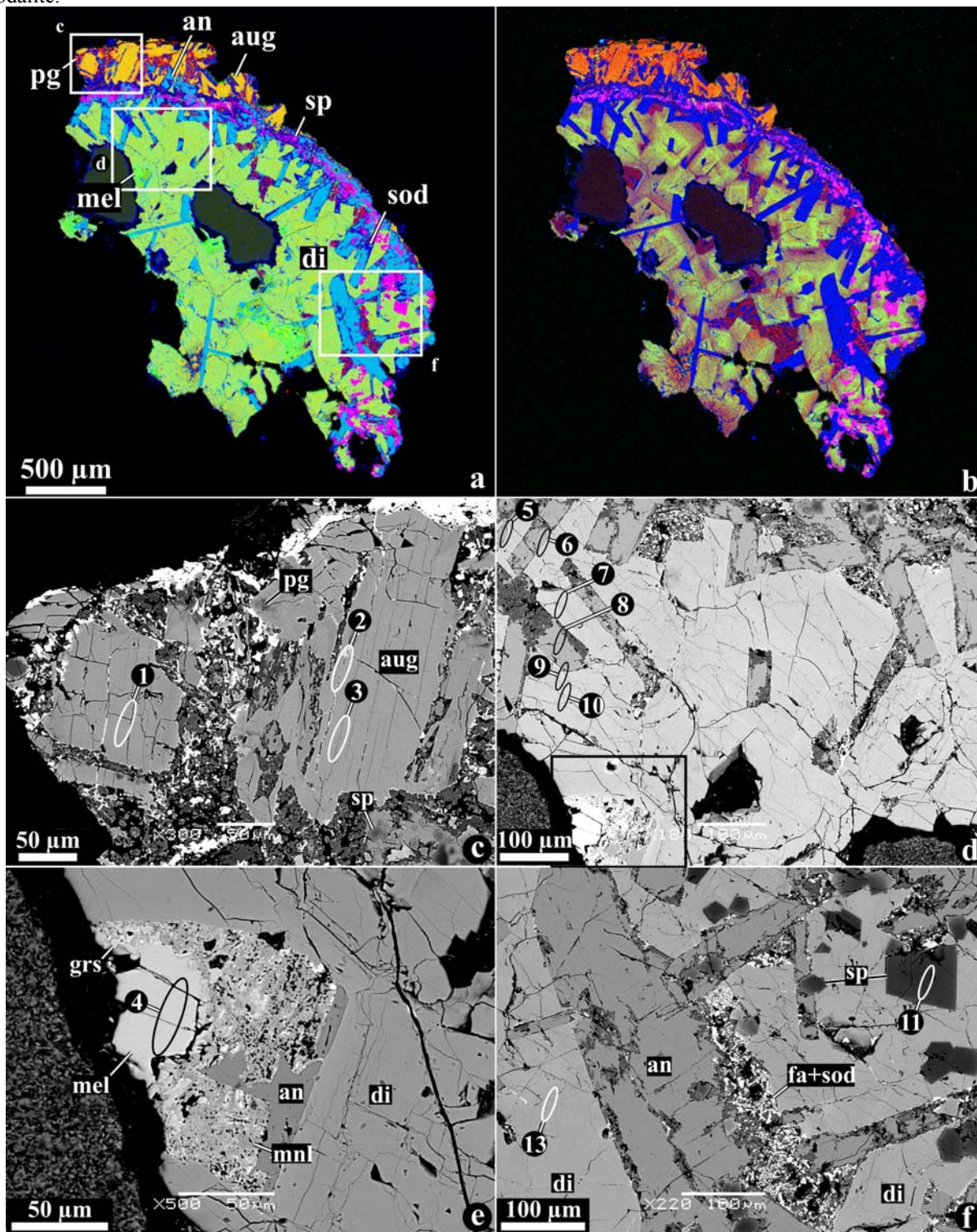


Fig. 6. (a) Combined elemental maps in Mg (red), Ca (green) and Al (blue) $K\alpha$ X-rays, (b) combined elemental maps in Mg (red), Ti (green) and Al (blue) $K\alpha$ X-rays, and (c-f) BSE images of a Type C ABC. Regions outlined and labeled in “b” are shown in detail in “c-f”. Ion probe spots are outlined and numbered; numbers correspond to those listed in Table 1. an = anorthite; aug = augite; Cr-sp = chromium spinel; di = Al,Ti-diopside, ol = olivine; grs = grossular; lpx = low-Ca pyroxene; mel = melilite; mes = mesostasis; mnl = monticellite; neph = nepheline; pl = anorthitic plagioclase; sf = sulfide; sod = sodalite; sp = spinel; wol = wollastonite.

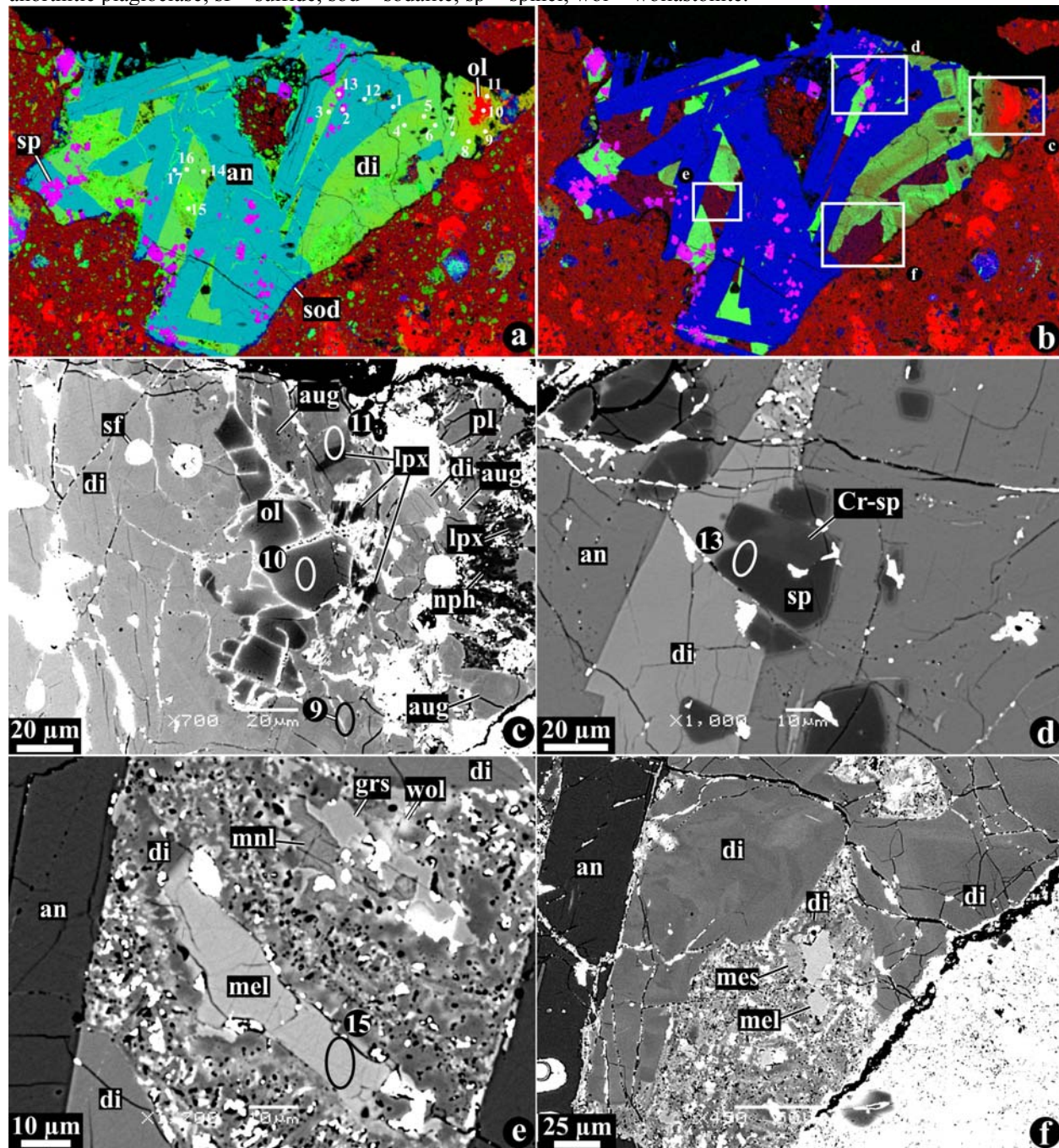


Fig. 7. Combined elemental maps in Mg (red), Ca (green) and Al (blue) K α X-rays, (b) combined elemental maps in Mg (red), Ti (green) and Al (blue) K α X-rays, and (c, d) BSE images of a Type C *TS26*. Regions outlined in and labeled “a” are shown in detail in “c” and “d”. Ion probe spots are outlined and numbered; numbers correspond to those listed in Table 1. an = anorthite; aug = augite; di = Al,Ti-diopside; ol = olivine; lpx = low-Ca pyroxene; mel = melilite; sod = sodalite; sp = spinel.

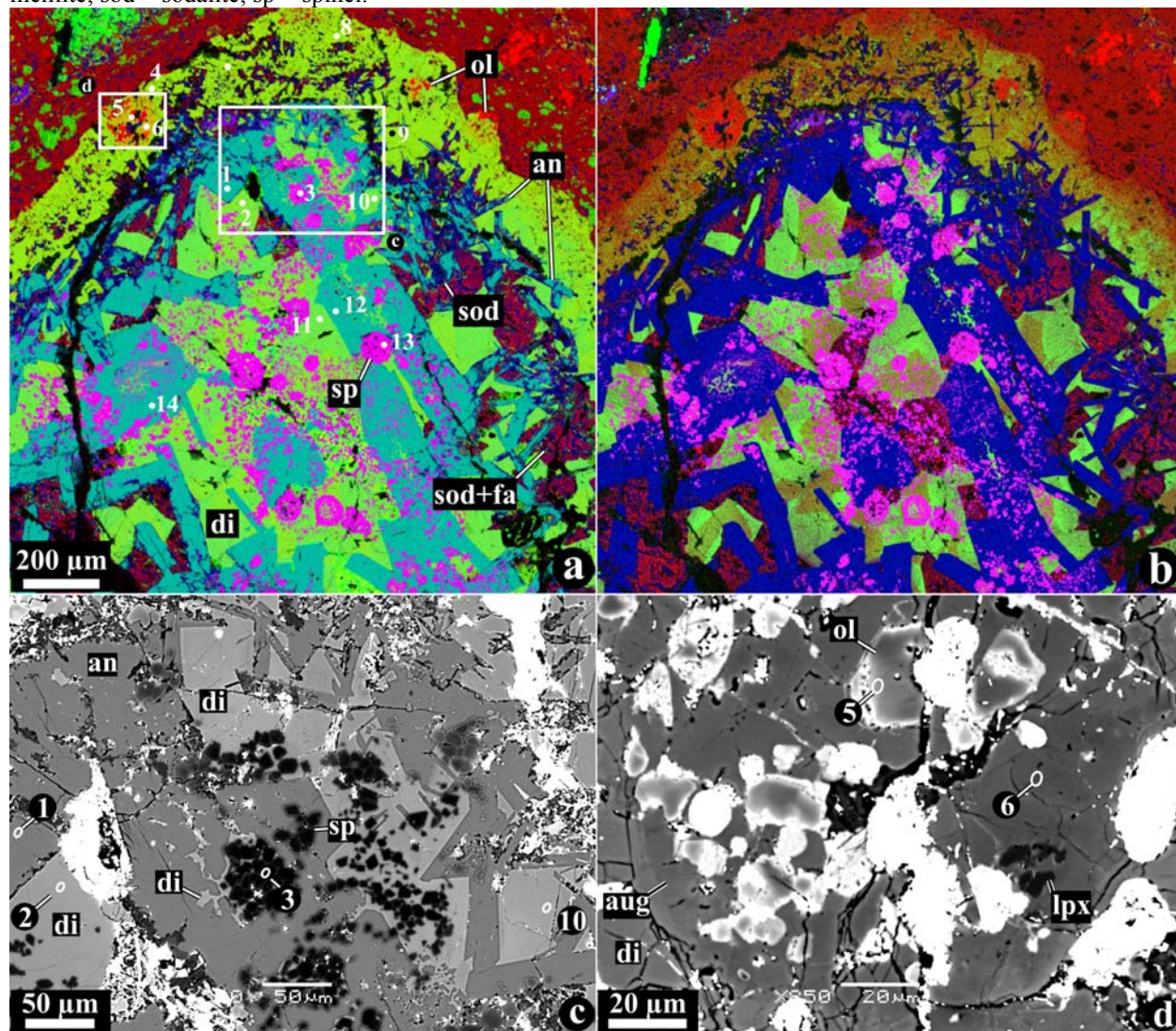


Fig. 8. Oxygen isotopic compositions of a Type C CAI 160. In “a”, data are plotted as $\delta^{17}\text{O}$ vs. $\delta^{18}\text{O}$; to illustrate variations in oxygen isotopic compositions of different minerals, in “b”, the same data, grouped by minerals, are plotted as deviations from the terrestrial fractionation line (TFL), $\Delta^{17}\text{O}$ ($= \delta^{17}\text{O} - 0.52 \times \delta^{18}\text{O}$). Carbonaceous chondrite anhydrous mineral (CCAM) line is shown for reference. an = anorthite; di = Al,Ti-diopside; grs+mnl = grossular + monticellite; mel = melilite; sp = spinel. Data were collected at CNRS/CRPG; error bars are 2σ .

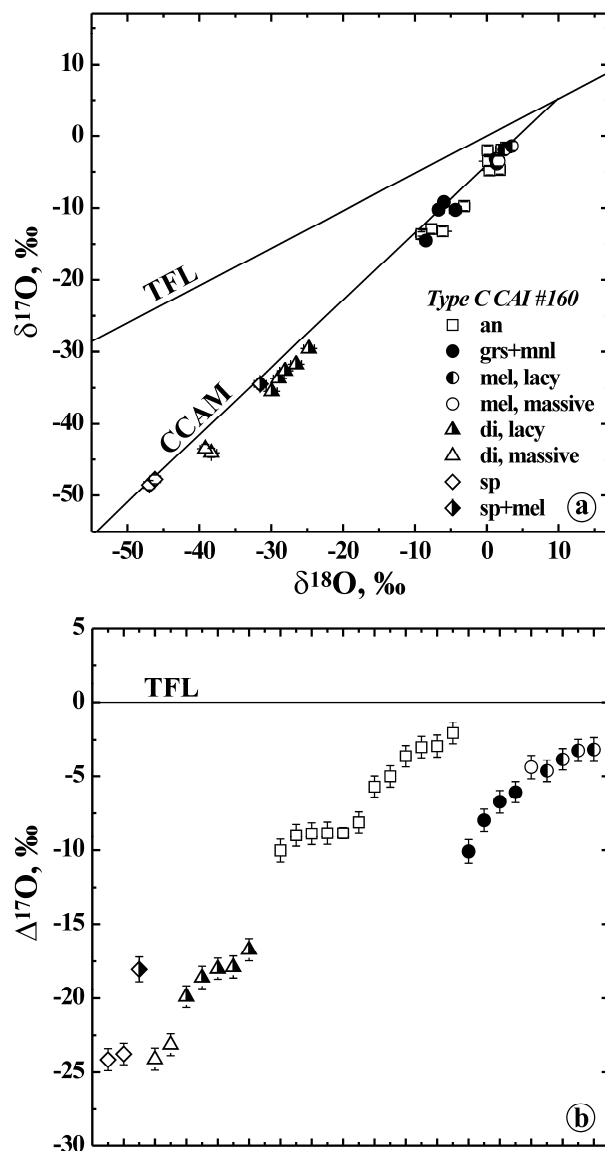


Fig. 9. Oxygen isotopic compositions of a Type C CAI 100 collected using CNRS-CRPG (a, b; 2σ error) and Hokudai (c, d; 2σ error) ion microprobes. In “a” and “b”, data are plotted as $\delta^{17}\text{O}$ vs. $\delta^{18}\text{O}$; in “c” and “d”, the same data, grouped by minerals, are plotted as $\Delta^{17}\text{O}$. an = anorthite; di = Al,Ti-diopside; fo = forsterite; grs = grossular; mel = melilite; mnl = monticellite; sp = spinel.

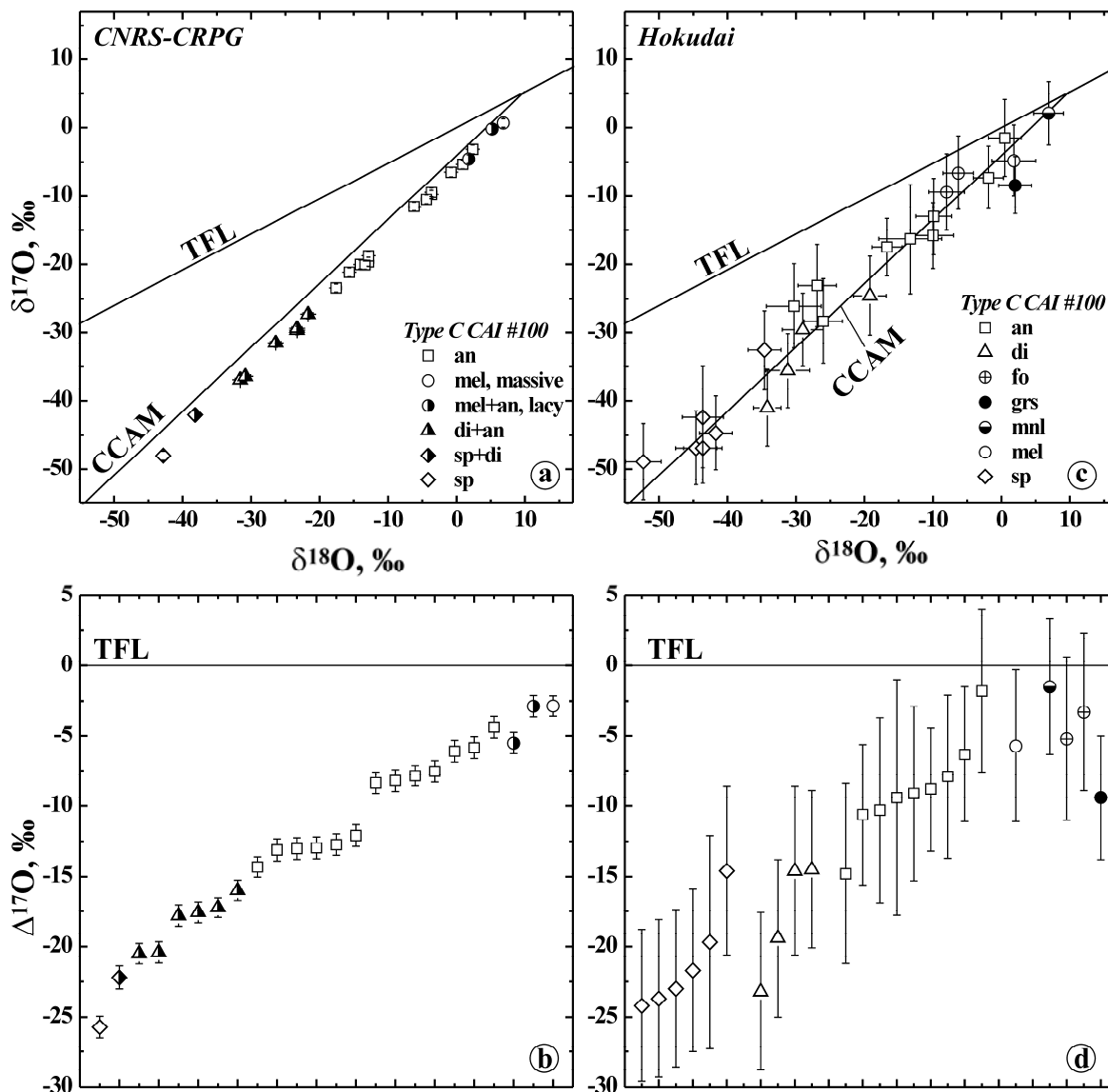


Fig. 10. Oxygen isotopic compositions of a the Type B-like and Type C portions of a CAI 6-1-72. In “a”, data are plotted as $\delta^{17}\text{O}$ vs. $\delta^{18}\text{O}$; to illustrate variations in oxygen isotopic compositions of different minerals, in “b”, the same data, grouped by minerals, are plotted as $\Delta^{17}\text{O}$. an = anorthite; di = Al,Ti-diopside; grs = grossular; mel = melilite; sp = spinel. Legends in the top left corner and the bottom right corner correspond to the data collected with the CNRS/CRPG and UH ion microprobes, respectively; error bars are 2σ .

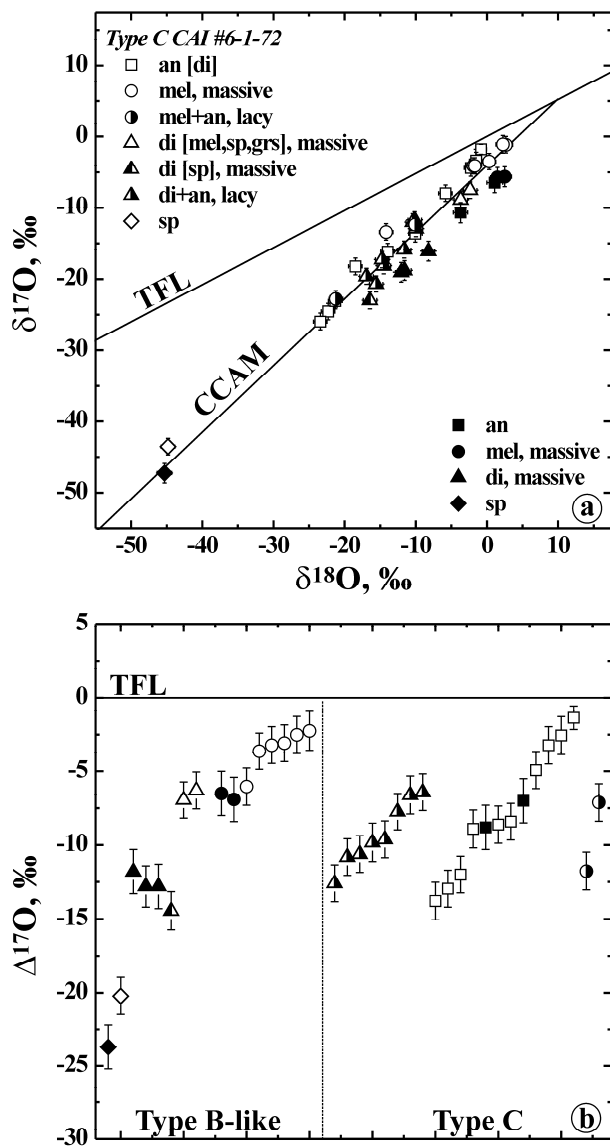


Fig. 11. Oxygen isotopic compositions of a Type C CAI CG5. In “a”, data are plotted as $\delta^{17}\text{O}$ vs. $\delta^{18}\text{O}$; in “b”, the same data are plotted as $\Delta^{17}\text{O}$. an = anorthite; di = Al,Ti-diopside; mel = melilite; sp = spinel. Data were collected at CNRS/CRPG; size of symbols correspond to 2σ errors.

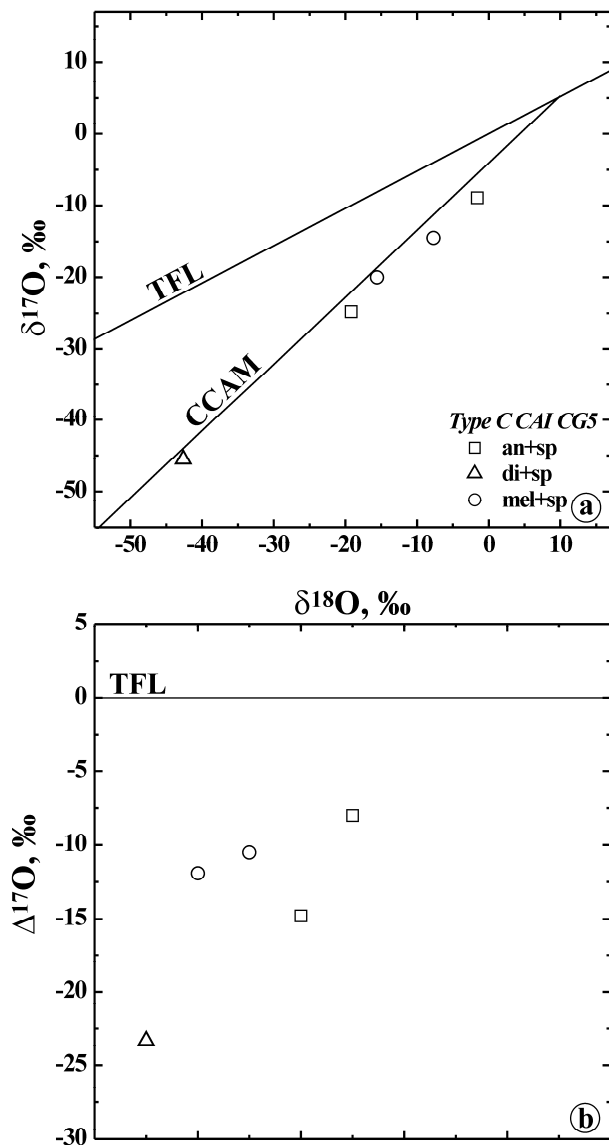


Fig. 12. Oxygen isotopic compositions of a Type C CAI #93 with a chondrule-like, igneous rim. In “a”, data are plotted as $\delta^{17}\text{O}$ vs. $\delta^{18}\text{O}$; in “b”, the same data, grouped by minerals, are plotted as $\Delta^{17}\text{O}$. an = anorthite; aug = augite; di = Al,Ti-diopside; mel = melilite; sec = secondary minerals; sp = spinel. Data were collected at CNRS/CRPG; error bars are 2σ .

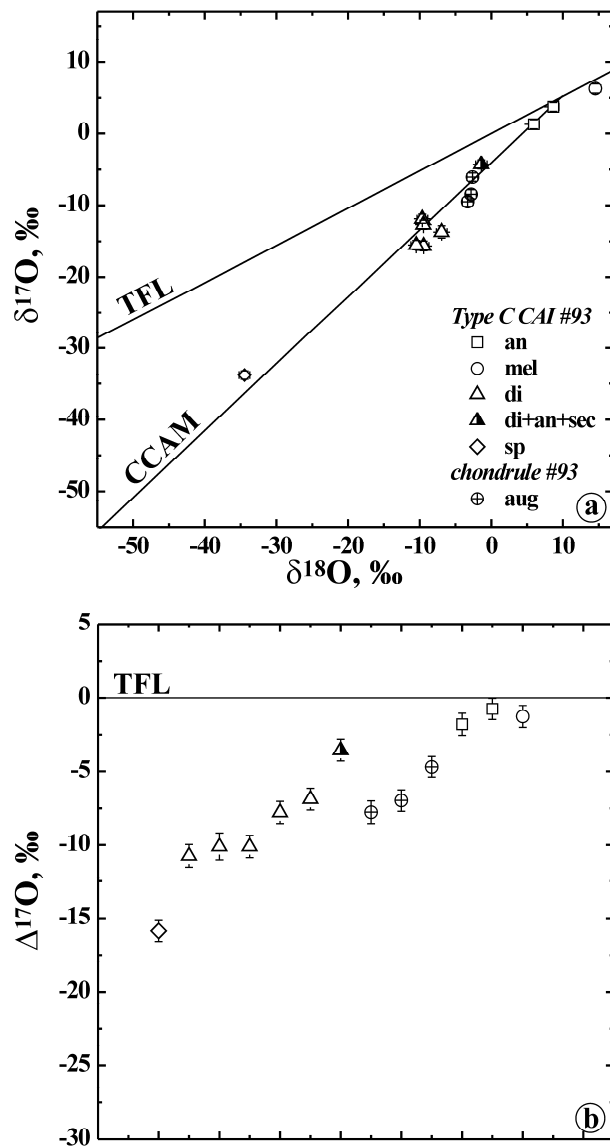


Fig. 13. Oxygen isotopic compositions of Type C CAIs ABC (a, b) and TS26 (c, d) with chondrule fragments in their peripheries (from Krot et al., 2007b). In “a” and “c”, data are plotted as $\delta^{17}\text{O}$ vs. $\delta^{18}\text{O}$; in “b” and “d”, the same data, grouped by minerals, are plotted as $\Delta^{17}\text{O}$. an = anorthite; aug = augite; Cr-sp = Cr-spinel; di = Al,Ti-diopside; lpx = low-Ca pyroxene; mel = melilite; ol = olivine; sp = spinel. Data were collected at Hokudai; error bars are 2σ .

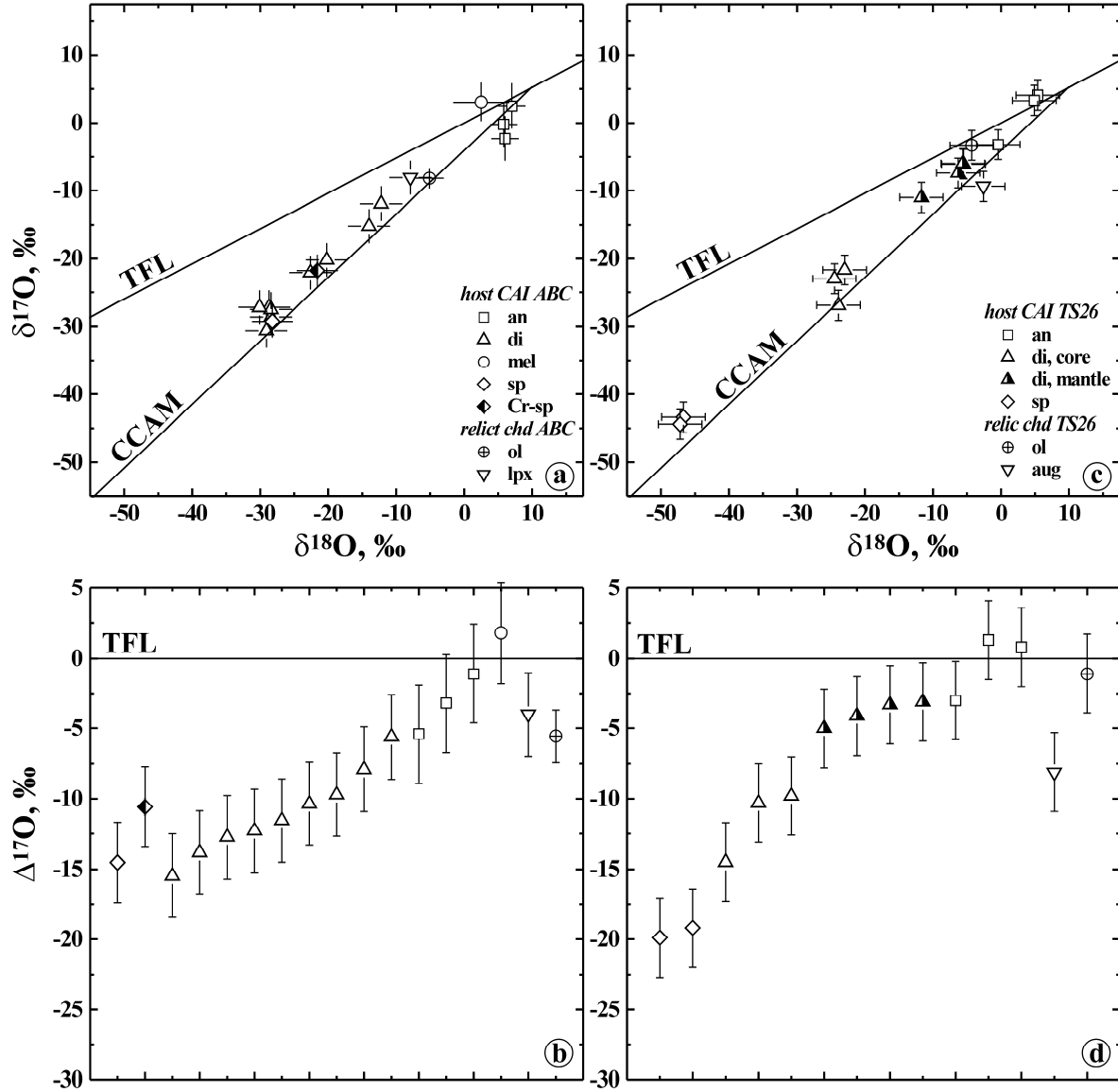


Fig. 14. a, b - Oxygen isotopic compositions of secondary magnetite (Mgt) and fayalite (Fa) in type I chondrules in the oxidized Bali-like CV chondrites Mokoia and Kaba (data from Choi et al., 2000; Hua et al., 2005; the latter are labeled by “*” in the legend to “b”). c, d - Oxygen isotopic compositions of secondary magnetite, Ca,Fe-pyroxenes (CaFe-px) and andradite (Andr) in various Allende components. Data for magnetite from Choi et al. (2000); data for Ca,Fe-pyroxenes, fayalitic olivine and andradite from Krot et al. (2000) and Cosarinsky et al. (2003). Error bars are 2σ .

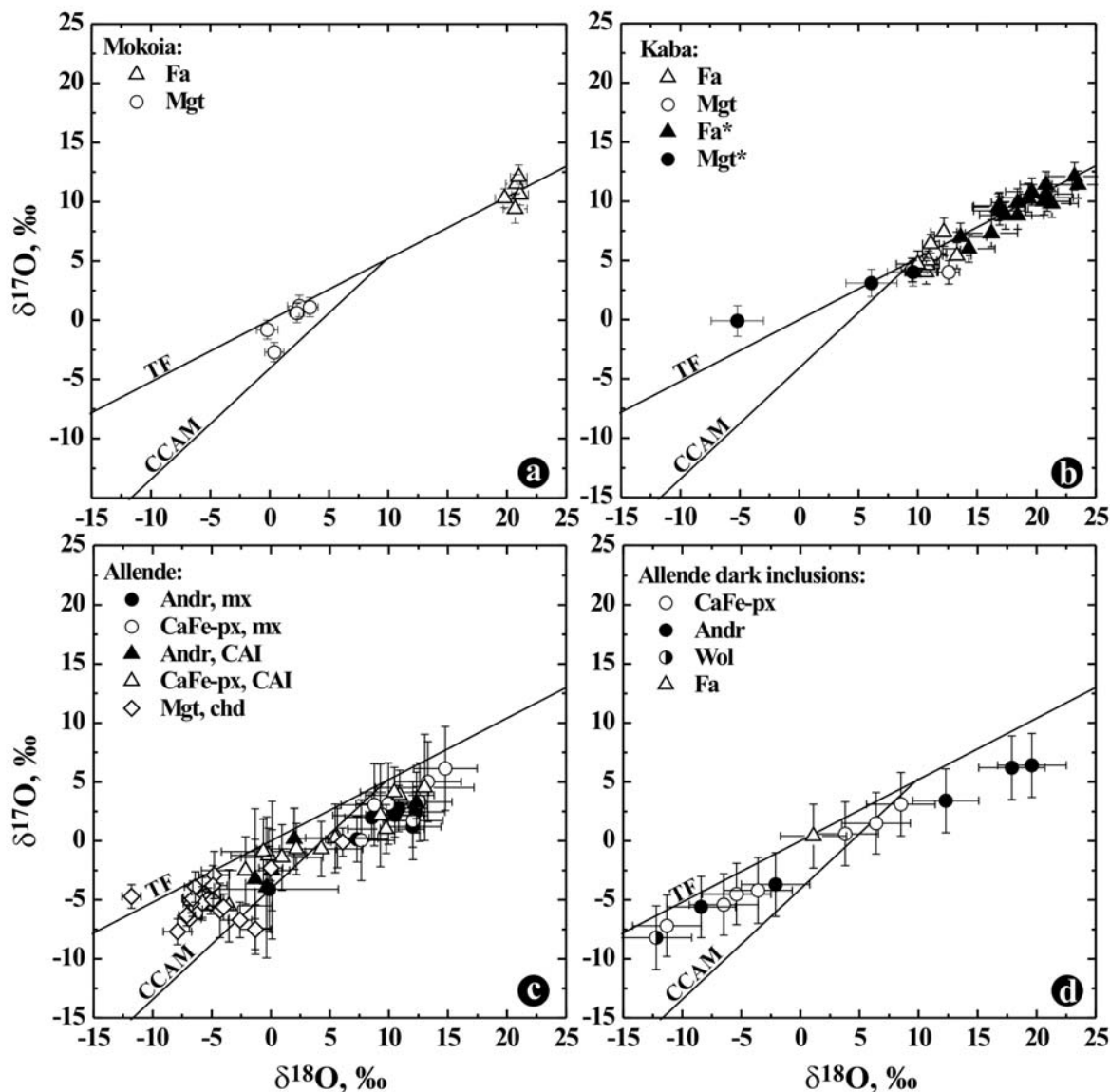


Table 1. Oxygen isotopic compositions of minerals from the Allende Type C CAIs.

CAI#, spot#	mineral	$\delta^{17}\text{O}$	2σ	$\delta^{18}\text{O}$	2σ	$\Delta^{17}\text{O}$	2σ
CAIs with lacy and massive melilite and fassaite							
#160							
182	di	-44.0	0.6	-38.3	0.8	-24.1	0.7
183	sp	-48.6	0.6	-47.0	0.7	-24.1	0.7
184	di	-43.5	0.6	-39.2	0.8	-23.1	0.7
185	sp	-47.8	0.6	-46.2	0.8	-23.7	0.7
186	sp [mel]	-34.4	0.7	-31.5	0.9	-18.0	0.8
187	an	-13.2	0.6	-6.1	0.8	-10.0	0.7
188	di+an [sp], lacy	-29.6	0.6	-24.8	0.7	-16.7	0.7
189	mel	-3.5	0.7	1.7	0.8	-4.4	0.8
190	di+an [sp], lacy	-33.7	0.6	-29.0	0.7	-18.6	0.8
191	di+an [sp], lacy	-31.7	0.6	-26.5	0.7	-17.9	0.7
192	di+an [sp], lacy	-32.6	0.6	-28.1	0.7	-18.0	0.7
193	an	-13.6	0.6	-9.1	0.8	-8.8	0.8
194	di+an [sp], lacy	-35.5	0.6	-29.9	0.8	-19.9	0.7
195	an	-13.6	0.6	-8.9	0.8	-9.0	0.7
196	an	-12.9	0.6	-7.7	0.8	-8.9	0.7
197	an	-1.6	0.6	2.7	0.8	-3.0	0.7
198	an	-4.7	0.6	1.8	0.8	-5.7	0.7
199	mel+an, lacy	-3.2	0.6	1.2	0.8	-3.8	0.7
200	mel+an, lacy	-1.9	0.7	2.4	0.8	-3.2	0.8
201	mel+an, lacy	-3.9	0.6	1.4	0.8	-4.6	0.7
202	an	-4.8	0.6	0.4	0.8	-5.0	0.7
203	an	-9.7	0.6	-3.1	0.8	-8.1	0.7
204	an	-3.5	0.6	0.2	0.8	-3.6	0.7
205	an	-1.9	0.6	2.0	0.8	-2.9	0.7
206	mel+an, lacy	-1.4	0.6	3.5	0.8	-3.2	0.8
207	grs	-14.5	0.6	-8.5	0.8	-10.1	0.8
208	grs	-9.2	0.6	-6.0	0.7	-6.1	0.7
209	an	-2.0	0.6	0.1	0.8	-2.0	0.7
210	grs	-10.2	0.6	-4.4	0.8	-8.0	0.8
211	grs	-10.2	0.6	-6.7	0.8	-6.7	0.8
#100							
82	an	-11.6	0.6	-6.2	0.7	-8.3	0.7
83	mel	0.7	0.6	6.8	0.7	-2.9	0.7
84	an	-3.1	0.7	2.4	0.7	-4.4	0.8
85	sp+di	-42.0	0.7	-38.2	0.7	-22.2	0.8
86	di [an]	-36.9	0.6	-31.6	0.7	-20.5	0.7
87	di [an]	-27.3	0.6	-21.7	0.7	-16.0	0.7

Table 1 (cont.)

CAI#, spot#	mineral	$\delta^{17}\text{O}$	2σ	$\delta^{18}\text{O}$	2σ	$\Delta^{17}\text{O}$	2σ
#100							
88	di+an [sp]	-31.5	0.7	-26.4	0.8	-17.8	0.8
89	an	-9.8	0.6	-3.7	0.7	-7.9	0.7
90	sp	-48.0	0.7	-42.8	0.8	-25.7	0.8
91	di+an	-36.4	0.6	-30.8	0.7	-20.4	0.7
92	di+an, lacy	-29.7	0.6	-23.3	0.7	-17.6	0.7
93	di+an, lacy	-29.3	0.6	-23.3	0.7	-17.2	0.7
94	an [di]	-18.8	0.7	-12.8	0.8	-12.1	0.8
95	an	-23.4	0.6	-17.6	0.8	-14.3	0.7
96	mel+an, lacy	-0.2	0.6	5.2	0.8	-2.9	0.8
97	mel+an, lacy	-4.6	0.6	1.8	0.7	-5.5	0.7
98	an	-6.5	0.7	-0.8	0.7	-6.1	0.8
99	an [sp]	-21.2	0.7	-15.6	0.8	-13.0	0.8
100	an	-9.4	0.7	-3.6	0.7	-7.5	0.8
101	an	-5.3	0.7	0.9	0.8	-5.8	0.8
102	an [sp]	-10.5	0.7	-4.4	0.7	-8.2	0.8
103	an [sp]	-20.0	0.6	-14.0	0.7	-12.7	0.8
104	an [sp]	-19.6	0.7	-12.8	0.7	-13.0	0.8
105	an [sp]	-20.1	0.7	-13.4	0.7	-13.1	0.8
#100^							
1	an	-15.8	4.8	-10.0	3.0	-10.6	5.0
2	sp	-46.9	5.4	-44.6	3.0	-23.7	5.6
3	mel	-4.8	5.2	1.8	3.2	-5.7	5.5
4	an	-7.3	4.6	-1.9	2.2	-6.3	4.7
5	sp	-46.9	5.2	-43.6	2.8	-24.2	5.4
6-1	fo	-9.4	5.6	-8.0	2.6	-5.2	5.8
6-2	fo	-6.6	5.4	-6.3	2.2	-3.3	5.5
7	an	-1.5	5.6	0.5	2.4	-1.8	5.7
8	sp	-44.7	5.4	-41.7	2.4	-23.0	5.5
9	grs	-8.4	4.2	2.0	2.4	-9.4	4.4
10	mnl	2.1	4.6	6.9	2.2	-1.5	4.7
16	an	-13.0	5.6	-9.9	2.6	-7.9	5.8
17	sp	-48.9	5.6	-52.3	2.6	-21.7	5.8
18	di	-35.6	5.4	-31.2	3.2	-19.4	5.7
19	an	-16.3	8.0	-13.3	4.6	-9.4	8.3
20	an	-26.1	6.2	-30.3	4.0	-10.3	6.5
21	di	-41.0	5.6	-34.2	2.0	-23.2	5.7
22	sp	-32.6	5.8	-34.6	2.4	-14.6	5.9
23	an	-17.5	4.2	-16.7	2.2	-8.8	4.4

Table 1 (cont.)

CAI#, spot#	mineral	$\delta^{17}\text{O}$	2σ	$\delta^{18}\text{O}$	2σ	$\Delta^{17}\text{O}$	2σ
#100[^] (cont.)							
24	an	-23.1	6.0	-26.9	2.8	-9.1	6.2
25	an	-28.3	6.2	-26.0	2.8	-14.8	6.4
26	di	-24.6	5.8	-19.2	2.4	-14.6	5.9
27	di	-29.6	5.4	-29.0	3.0	-14.5	5.6
28	sp	-42.4	7.4	-43.6	3.0	-19.7	7.6
#6-1-72							
Type C portion with lacy melilite and Al,Ti-diopside							
17*	an [di]	-6.5	1.4	1.1	1.1	-7.0	1.5
18*	an	-10.7	1.4	-3.7	1.0	-8.8	1.5
32	an	-1.8	0.7	-0.8	0.8	-1.4	0.8
46	an [di]	-13.6	1.1	-10.1	1.0	-8.4	1.2
47	di+an, lacy	-15.9	1.2	-11.6	1.0	-9.8	1.3
48	di+an, lacy	-18.1	1.1	-14.5	1.0	-10.6	1.2
49	di+an, lacy	-19.6	1.1	-16.9	1.0	-10.8	1.2
50	an	-7.9	1.2	-5.8	1.0	-4.9	1.3
51	an [di]	-16.2	1.2	-14.0	1.0	-8.9	1.3
52	di+an, lacy	-20.7	1.1	-15.6	1.0	-12.6	1.2
53	di+an, lacy	-17.3	1.1	-14.7	1.0	-9.6	1.3
54	di+an, lacy	-12.9	1.1	-10.0	1.0	-7.7	1.2
55	an [di]	-24.6	1.1	-22.3	1.0	-13.0	1.2
56	an [di]	-26.0	1.2	-23.4	1.0	-13.8	1.3
57	an [di]	-23.1	1.1	-21.3	1.0	-12.0	1.2
58	an [di]	-4.4	1.2	-2.2	1.0	-3.2	1.3
59	an [di]	-3.3	1.2	-1.5	1.0	-2.6	1.3
60	mel [sp,grs]	-22.8	1.2	-21.2	1.0	-11.8	1.3
61	an [di]	-18.2	1.2	-18.5	1.0	-8.6	1.3
62	di+an, lacy	-11.7	1.1	-10.1	1.0	-6.4	1.2
63	mel+an, lacy	-12.4	1.2	-10.1	1.0	-7.1	1.3
64	di+an, lacy	-12.0	1.2	-10.4	1.0	-6.6	1.3
Type B-like portion with massive melilite and Al,Ti-diopside							
16*	sp	-47.3	1.4	-45.3	1.0	-23.7	1.5
19*	mel	-5.6	1.4	2.5	0.9	-6.9	1.5
20*	mel	-5.7	1.4	1.4	0.9	-6.5	1.5
21*	di	-18.8	1.4	-11.6	0.9	-12.8	1.5
22*	di	-19.0	1.4	-12.0	0.8	-12.8	1.4
23*	di	-16.1	1.4	-8.2	0.9	-11.8	1.5
33	mel [sp,an]	-13.4	1.2	-14.2	1.0	-6.0	1.3
34	di [mel,sp,grs]	-8.9	1.1	-3.7	1.0	-6.9	1.2

Table 1 (cont.)

CAI#, spot#	mineral	$\delta^{17}\text{O}$	2σ	$\delta^{18}\text{O}$	2σ	$\Delta^{17}\text{O}$	2σ
<i>Type B-like portion with massive melilite and Al,Ti-diopside (cont.)</i>							
35	di [mel,sp,grs]	-7.5	1.1	-2.4	1.0	-6.3	1.2
36	di [sp]	-23.0	1.2	-16.4	1.0	-14.4	1.3
40	sp	-43.5	1.2	-44.8	1.0	-20.2	1.3
41	mel [grs]	-4.1	1.1	-1.9	1.0	-3.1	1.2
42	mel [grs]	-3.5	1.1	0.3	1.0	-3.6	1.2
43	mel [grs]	-4.1	1.1	-1.7	1.0	-3.2	1.2
44	mel	-1.1	1.2	2.7	1.0	-2.5	1.3
45	mel	-1.1	1.2	2.2	1.0	-2.3	1.3
CAI CG5 with massive melilite, Al,Ti-diopside and anorthite							
110	di+sp	-45.5	0.3	-42.6	0.4	-23.3	0.4
111	mel+sp	-20.0	0.3	-15.6	0.4	-11.9	0.4
112	mel+sp	-14.5	0.4	-7.7	0.4	-10.5	0.4
113	an+sp	-8.9	0.4	-1.6	0.4	-8.0	0.4
114	an+sp	-24.8	0.4	-19.2	0.4	-14.8	0.5
CAIs with chondrule fragments in their peripheries and a chondrule-like igneous rim							
<i>ABC</i>							
1	an	-2.3	3.3	6.0	2.0	-5.4	3.5
2	sp	-29.2	2.4	-28.2	3.0	-14.5	2.9
3	di, core	-28.6	2.5	-28.4	3.1	-13.8	3.0
4	di, core	-22.1	2.5	-22.6	3.1	-10.4	3.0
5	di, core	-20.2	2.5	-20.2	3.1	-9.7	3.0
6	di, mantle	-27.2	2.5	-28.7	3.1	-12.3	3.0
7	di, mantle	-30.6	2.5	-29.1	3.1	-15.5	3.0
8	di, mantle	-15.2	2.5	-14.0	3.1	-7.9	3.0
9	di, mantle	-11.9	2.5	-12.2	3.1	-5.6	3.0
10	ol	-8.2	1.5	-5.1	2.1	-5.5	1.9
11	lpx [aug]	-8.1	2.5	-7.9	3.1	-4.0	3.0
12	an	-0.2	3.3	5.8	2.0	-3.2	3.5
13	Cr-sp	-21.8	2.4	-21.6	3.0	-10.6	2.9
14	di, core	-27.5	2.5	-28.4	3.1	-12.7	3.0
15	mel	3.1	2.8	2.5	4.1	1.8	3.6
16	di, core	-27.2	2.5	-30.1	3.1	-11.6	3.0
17	an	2.5	3.3	7.0	2.0	-1.1	3.5
<i>TS26</i>							
1	an	-3.2	2.2	-0.4	3.2	-3.0	2.8
2	di, core	-26.9	2.2	-23.9	3.2	-14.5	2.8

Table 1 (cont.)

CAI#, spot#	mineral	$\delta^{17}\text{O}$	2σ	$\delta^{18}\text{O}$	2σ	$\Delta^{17}\text{O}$	2σ
<i>TS26 (cont.)</i>							
3	sp	-43.4	2.2	-46.7	3.2	-19.2	2.8
4	di, mantle	-7.4	2.2	-6.3	3.2	-4.1	2.8
5	ol	-3.3	2.2	-4.3	3.2	-1.1	2.8
6	aug	-9.4	2.2	-2.6	3.2	-8.1	2.8
7	di, mantle	-6.1	2.2	-5.5	3.2	-3.3	2.8
8	di, mantle	-6.0	2.2	-5.6	3.2	-3.1	2.8
9	di, mantle	-11.0	2.2	-11.7	3.2	-5.0	2.8
10	di, core	-23.0	2.2	-24.5	3.2	-10.3	2.8
11	di, core	-21.7	2.2	-23.0	3.2	-9.8	2.8
12	an	4.1	2.2	5.4	3.2	1.3	2.8
13	sp	-44.4	2.2	-47.2	3.2	-19.9	2.8
14	an	3.3	2.2	4.9	3.2	0.8	2.8
#93							
1	aug	-9.5	0.7	-3.3	0.7	-7.8	0.8
2	aug	-6.1	0.6	-2.6	0.7	-4.7	0.7
3	aug	-8.4	0.6	-2.8	0.8	-7.0	0.7
4	mel	6.3	0.6	14.5	0.8	-1.3	0.8
5	di+an	-13.7	0.8	-6.9	0.8	-10.1	0.9
6	di+an+sec	-4.3	0.6	-1.4	0.8	-3.6	0.7
7	di	-15.5	0.7	-10.5	0.7	-10.1	0.8
8	an [sec]	3.8	0.6	8.7	0.8	-0.8	0.7
9	di [an]	-11.9	0.6	-9.6	0.7	-6.9	0.7
10	di	-12.7	0.6	-9.5	0.8	-7.8	0.7
11	sp	-33.8	0.6	-34.4	0.7	-15.9	0.7
12	an	1.3	0.6	5.9	0.8	-1.8	0.7
13	lpx [aug]	-15.7	0.7	-9.4	0.8	-10.7	0.8

an = anorthite; aug = augite; Cr-sp = chromian spinel; di = Al,Ti-diopside; grs = grossular; lpx = low-Ca pyroxene; mel = melilite; mnl = monticellite; ol = olivine; sec = secondary minerals; sp = spinel. Minerals occupying <10 vol% of analyzed area are listed in brackets. Data for CAIs ABC, TS26 and 100[^] were collected at Hokudai; data collected at UH are indicated by *; other data were collected at CNRS/CRPG.